Submitted to the International Europhysics Conference on High Energy Physics EPS-HEP99
Tampere, Finland, 15-21 July 1999

Measurement of Neutral and Charged Current Cross-Sections in Positron-Proton Collisions at Large Momentum Transfer

H1 Collaboration

Abstract

The inclusive single and double differential cross-sections for neutral and charged current processes with four-momentum transfer squared Q^2 between 150 and $30\,000$ GeV^2 and with Bjorken x between 0.0032 and 0.65 are measured in e^+p collisions. The data were taken with the H1 detector at HERA between 1994 and 1997, and they correspond to an integrated luminosity of $35.6\ \mathrm{pb}^{-1}$. The Q^2 evolution of the parton densities of the proton is tested, yielding no significant deviation from the prediction of perturbative QCD. The proton structure function $F_2(x, Q^2)$ is determined. An extraction of the u and d quark distributions at high x is presented. At high Q^2, electroweak effects of the heavy bosons Z° and W are observed and found to be consistent with Standard Model expectation.

Abstract: 157ai
Parallel session: 2,6
Plenary session: 3,6

Electronic Access: http://www-h1.desy.de/publications/

1 Introduction

The deep-inelastic scattering (DIS) of leptons off nucleons has played a fundamental role in understanding the structure of matter and in the foundation of the Standard Model. The first DIS measurements revealed the existence of partons in the proton [1] and opened the way to the development of Quantum Chromodynamics (QCD) as the theory of strong interactions. The establishment of electroweak theory followed the observation of neutral current neutrino scattering [2]. Subsequent (fixed target) DIS experiments [3, 4, 5] have helped to constrain the electroweak parameters of the Standard Model and the partonic structure of the proton.

At HERA, the first electron-proton (ep) collider ever built, the study of DIS has been further pursued since 1992. There are two contributions to DIS, both of which can be measured at HERA, neutral current (NC) interactions, $ep \to eX$, and charged current (CC) interactions, $ep \to \nu X$. In the Standard Model a photon (γ) or a Z° boson is exchanged in a NC interaction, and a W boson is exchanged in a CC interaction. DIS can be described by the four-momentum transfer squared Q^2, Bjorken x and inelasticity y defined as

$$Q^2 = -q^2 \equiv (k - k')^2 \qquad\qquad x = \frac{Q^2}{2p \cdot q} \qquad\qquad y = \frac{p \cdot q}{p \cdot k} \tag{1}$$

with $k(k^{'})$ and p being the four-momentum of the incident (scattered) lepton and proton. The centre-of-mass energy $\sqrt{s}$ of the ep interaction is given by $s \equiv (p + k)^2 = Q^2/xy$ when neglecting the proton and positron masses.

In this paper, the high Q^2 range of the measurements is extended up to $30\,000\ \mathrm{GeV}^2$. The fixed target experiments covered the kinematic range up to $Q^2 = 250\ \mathrm{GeV}^2$ and down to $x \approx 10^{-2}$. Previous results by the HERA experiments, H1 and ZEUS, extended to higher values of $Q^2 = 5000\ \mathrm{GeV}^2$ and to lower values of $x \approx 10^{-5}$ at low Q^2 [6, 7]. These extensions in kinematic domain were made possible by the HERA positron and proton beam energies of $E_e = 27.6\ \mathrm{GeV}$ and $E_p = 820\ \mathrm{GeV}$ and consequently large $\sqrt{s} \approx 300\ \mathrm{GeV}$.

For NC interactions at low x, the measurements of the proton structure function F_2 revealed [8, 9] a strong rise with decreasing x, which can be accommodated by perturbative QCD in the form of Next-to-Leading Order (NLO) DGLAP [10] evolution equations. The kinematic reach in x at high Q^2, allowed cross-sections which are directly related to the valence quark distributions of the proton to be measured albeit with limited precision. For CC interactions measurements of e^-p and e^+p single differential cross-sections extended the results obtained in fixed target neutrino and antineutrino scattering to higher Q^2 [11, 12]. The measurements were used to determine the W propagator mass M_W.

In this paper measurements of the NC and CC cross-sections at high Q^2 are presented. The results are obtained using e^+p data taken between 1994 and 1997. The integrated luminosity of $35.6\ \mathrm{pb}^{-1}$ is more than a factor of 10 greater than for previously published measurements of NC and CC cross-sections by H1 [6, 11]. The increase in integrated luminosity enables both the influence of the Z° boson in NC interactions and the helicity structure of the CC interaction to be tested in the high Q^2 domain. The behaviour of the NC and CC cross-sections at the highest Q^2 is of particular interest following the observation by H1 and ZEUS [13, 14] of an excess over Standard Model expectation of NC events at Q^2 greater than $15\,000\ \mathrm{GeV}^2$ using the e^+p data taken between 1994 and 1996. A detailed analysis of the significance of this excess using the complete e^+p data set used here is presented in [15]. Recently measurements of the NC and CC cross-sections at high Q^2 have been reported by the ZEUS experiment [16, 17].

This paper consists of five sections. In section 2 the experimental technique used for the measurements is presented. In section 3 the procedures used for the cross-section measurement, and the QCD analysis which is used subsequently to interpret the data, are described. In section 4 the cross-section measurements and their interpretation are presented. The paper is summarized in section 5.

2 Experimental Technique

2.1 Kinematic Reconstruction

The measurement of the differential DIS cross-sections relies on the precise determination of the kinematic variables of each event. Different reconstruction methods are used for CC and NC interactions.

For CC interactions the kinematic variables can only be reconstructed using the hadronic final state since the neutrino (ν) is not detected. To characterize the hadronic final state, it is convenient to introduce the quantity Σ, the transverse momentum $P_{T,h}$ and the inclusive hadronic angle γ_h defined by

$$\Sigma = \sum_i (E_i - p_{z,i}) \qquad P_{T,h} = \sqrt{(\sum_i p_{x,i})^2 + (\sum_i p_{y,i})^2} \qquad \tan\frac{\gamma_h}{2} = \frac{\Sigma}{P_{T,h}}. \tag{2}$$

Here E_i and $p_{z,i}$ are the energy and longitudinal momentum component of a particle i, and $p_{x,i}$, $p_{y,i}$ are its momentum components in the plane orthogonal to the z axis[1]. The summation is carried over all hadronic final state particles whose masses are neglected[2]. The kinematic variables are then obtained from [18]:

$$y_h = \frac{\Sigma}{2\,E_e} \qquad Q_h^2 = \frac{P_{T,h}^2}{1-y_h} \qquad x_h = \frac{Q_h^2}{s\,y_h}. \tag{3}$$

This "hadron method" (h method) gives moderate precision in the reconstruction of the kinematic variables because of particle losses in the beam pipe and fluctuations of the detector response to hadronic final state particles. It is thus used only for the CC interactions.

For NC interactions, different methods of determining the kinematic variables are possible since there is redundant information with the simultaneous reconstruction of the scattered positron and of the hadronic final state. The choice of the method determines the corrections due to resolution and radiative effects, and the size of the systematic errors. The energy E'_e and the polar angle θ_e of the scattered positron are used to determine, in the "electron method" (e method), the variables

$$y_e = 1 - \frac{E'_e(1-\cos\theta_e)}{2\,E_e} \qquad Q_e^2 = \frac{P_{T,e}^2}{1-y_e} \qquad x_e = \frac{Q_e^2}{s\,y_e} \tag{4}$$

[1]The forward direction and the positive z axis are defined at HERA as the proton beam direction.

[2]The $p_{x,h}$ and $p_{y,h}$ components of the vectorial hadronic transverse momentum $\vec{P}_{T,h}$ are defined using the same summation on $p_{x,i}$ and $p_{y,i}$ respectively.

with $P_{T,e} = E'_e \sin\theta_e$. The e method has an excellent resolution in Q^2 and in x at large y. The Σ method [19] makes use of the positron and the hadronic final state variables. It has a better resolution in x at low y and is less sensitive to radiative effects since

$$y_\Sigma = \frac{\Sigma}{E{-}p_z} \qquad \text{with} \qquad E{-}p_z = \Sigma + E'_e(1-\cos\theta_e) \tag{5}$$

does not depend on the energy of the incoming positron. A combination of the e and Σ methods, the $e\Sigma$ method [19], is thus used to optimize the kinematic reconstruction in the NC measurement: Q^2 is taken from the e method and x from the Σ method. Both these variables display a good resolution in the complete kinematic range and the radiative corrections remain small compared to those of the e method. The $e\Sigma$ formulae are

$$y_{e\Sigma} = \frac{2E_e}{E{-}p_z} y_\Sigma \qquad Q^2_{e\Sigma} = \frac{P^2_{T,e}}{1-y_e} \qquad x_{e\Sigma} = \frac{P^2_{T,e}}{s\; y_\Sigma(1-y_\Sigma)}. \tag{6}$$

2.2 Detector and Trigger

The H1 detector [20] is a nearly hermetic multi-purpose apparatus built to investigate ep scattering. The high Q^2 cross-section measurements reported here rely primarily on the tracking system, on the Liquid Argon (LAr) calorimeter, on the luminosity detectors, and to a lesser extent on the backward calorimeter. These components are described briefly below.

The tracking system includes the central and forward tracking chambers. These detectors are placed around the beam pipe at z positions between -1.5 and 2.5 m. A superconducting solenoid, which surrounds both the tracking system and the LAr calorimeter, provides a uniform magnetic field of 1.15 T. The central jet chamber (CJC) consists of two concentric drift chambers covering a polar angular range from $25°$ to $155°$. Particles crossing the CJC are measured with a transverse momentum resolution of $\delta P_T/P_T < 0.01 \cdot P_T/\mathrm{GeV}$. To improve the determination of the z coordinate of the tracks, two polygonal drift chambers with wires perpendicular to the beam axis placed at radii of 18 (CIZ) and 47 cm (COZ) are used. The forward tracking detector measures charged particles emitted in an angular range from $7°$ to $20°$. It is used in this analysis to determine the interaction vertex for events with no track in the CJC.

In high Q^2 NC events the scattered positron energy and most of the hadronic final state transverse energy are measured in the LAr calorimeter [21] which covers an angular region between $4°$ and $154°$. The calorimeter consists of an electromagnetic section with lead absorber plates and a hadronic section with stainless steel absorber plates. Both sections are highly segmented in the transverse and longitudinal directions with about $44\ 000$ cells in total. The electromagnetic part has a depth between 20 and 30 radiation lengths ($X_\circ$). The total depth of the calorimeter varies between 4.5 and 8 interaction lengths (λ_I). The systematic uncertainty of the electromagnetic (hadronic) energy scale of the LAr calorimeter is between 0.7 and 3% (2%) (section 2.6).

In the backward region, a lead/scintillating fibre calorimeter (SPACAL) [22] was installed in 1995 to replace the previous lead/scintillator electromagnetic calorimeter (BEMC). The new calorimeter has both an electromagnetic and a hadronic section with a total depth of about $2\lambda_I$, compared with the $1\lambda_I$ depth of the BEMC. Together with the LAr calorimeter, its angular acceptance ($154° < \theta < 177.8°$) makes possible a complete coverage for the detection of the hadronic final state in the H1 apparatus apart from the remnants of the proton. The uncertainty on the measurement of hadronic energy in the SPACAL is 7%, compared with 15% for the BEMC which was operational when the 1994 data were taken. The influence of the backward calorimeter on the analysis presented here is small.

The LAr and backward calorimeters are surrounded by the Instrumented Iron [20] which is used for muon identification and for the measurement of hadronic energy leaking from the other calorimeters. In this analysis, it is mainly used to reject muon induced background.

The ep luminosity is determined by comparison of the QED cross-section for the Bremsstrahlung reaction $ep \to ep\gamma$ with the measured event rate. The photon is detected in a calorimeter (photon "tagger") close to the beampipe which is situated at a large distance from the main detector ($z = -103$ m). The precision of the luminosity determination is 1.5% [23].

An electron tagger is placed at $z = -33$ m adjacent to the beam pipe. It is used to check the luminosity measurement and to provide information on $ep \to eX$ events at very low Q^2 (photoproduction) where the positron scatters through a small angle ($\pi - \theta_e < 5$ mrad).

The "trigger" of the high Q^2 events is mainly based on the the LAr calorimeter. In NC events the positron initiates a trigger "tower" [20, 21] of electromagnetic energy which points towards the event vertex. Above the threshold energy of the analysis (11 GeV) the trigger efficiency is greater than $99.5 \pm 0.5\%$. For CC events the missing transverse momentum $P_T^{\rm miss}$ as determined from the vector sum of the calorimeter towers[3] is used as the trigger. During 1997 data taking, a trigger which used track information supplemented the $P_T^{\rm miss}$ trigger in events with small missing transverse momentum and large angles of the hadrons. The combined efficiency of these triggers [24] reaches $98 \pm 2\%$ for a missing transverse momentum $P_T^{\rm miss}$ above 25 GeV, and is $50 \pm 8\%$ at the minimum $P_T^{\rm miss}$ of the analysis (12 GeV).

2.3 Event Simulation

In order to determine acceptance corrections and background contributions for the DIS cross-section measurements, the detector response to events produced by various Monte Carlo generation programs is simulated in detail using a program based on GEANT [25]. These simulated events are then subject to the same reconstruction and analysis chain as the real data.

DIS processes are generated using the DJANGO [26] program which is based on HERACLES [27] for the electroweak interaction and on LEPTO [28], using the colour dipole model as implemented in ARIADNE [29] to generate the QCD dynamics. The JETSET program is used for the hadron fragmentation [30]. The implementation of HERACLES in DJANGO includes the real Bremsstrahlung from the positron and the effects from vacuum polarization [31]. The simulated events are produced with the MRSH [32] parton distributions, reweighted to the H1 NLO QCD Fit described in section 3.2 which then gives a better description of the data.

The NC (CC) analysis makes use of a sample of simulated events corresponding to an integrated luminosity of about 3 (75) times that of the data. At $Q^2 > 1000$ GeV^2 and $x > 0.3$ additional samples of simulated events are included, which amount to between 10 and 1000 times the integrated luminosity of the data .

The main background contribution to NC and CC processes is due to photoproduction (γp) events. These are simulated using the PYTHIA [33] generator with GRV leading order parton

[3]For CC events this scalar quantity $P_T^{\rm miss}$ is equal to $P_{T,h}$.

distribution functions for the proton and photon [34]. This background is described in detail in section 2.5.2.

Further potential background contributions resulting from the following ep processes have been simulated: 1) elastic and inelastic QED Compton events can fake NC processes and are generated by the COMPTON program [35]; 2) elastic and inelastic $\gamma\gamma$ processes producing pairs of leptons (l), $ep \to ep\, l^+\, l^- (eX\ l^+\ l^-)$, are generated using the LPAIR program [36] (processes with $l^\pm = e^\pm$ can contribute to the NC sample, while processes with $l^\pm = \mu^\pm$ are more likely to contribute in the CC sample); 3) prompt photon production with $\gamma - e$ misidentification can fake NC events and is generated as a dedicated PYTHIA sample; 4) real production of heavy gauge bosons, $ep \to eXW^\pm(eXZ)$, followed by leptonic decays of the W or Z is generated using the EPVEC [37] program. These processes were found to produce only a small ($\lesssim$1%) contamination in any bin[4] of this analysis. They have been taken into account and will not be discussed henceforth.

2.4 Event Selection

For CC events the selection is based on the observation of large $P_T^{\rm miss}$, which is assumed to be the transverse momentum p_T^ν carried by the outgoing neutrino. For NC events it is based on the identification of a scattered positron with large $P_{T,e}$. For both CC and NC events an event vertex, which is reconstructed using central or forward tracks, is required to be within ± 35 cm of its nominal position. Fiducial (NC) and kinematic cuts (CC and NC) are then applied. The reconstruction of the kinematic variables for each selection follows the methods described in section 2.1 and uses the measurements of the positron and the hadronic final state, which are described in section 2.6.

CC events are selected as follows:

- the $P_T^{\rm miss}$ is required to be greater than 12 GeV;
- inelasticity in the range $0.03 < y_h < 0.85$ is required to restrict the measurement to a region where the kinematic reconstruction is precise;
- the ratio V_{ap}/V_p is required to be less than 0.15 to reject photoproduction background; V_p and V_{ap} are respectively the transverse energy flow parallel and antiparallel to $\vec{P}_{T,h}$; they are determined from the transverse momentum vectors $\vec{P}_{T,i}$ of all the particles i which belong to the hadronic final state according to

$$V_p = \sum_i \frac{\vec{P}_{T,h} \cdot \vec{P}_{T,i}}{P_{T,h}} \qquad \text{for} \qquad \vec{P}_{T,h} \cdot \vec{P}_{T,i} > 0 \tag{7}$$

$$V_{ap} = -\sum_i \frac{\vec{P}_{T,h} \cdot \vec{P}_{T,i}}{P_{T,h}} \qquad \text{for} \qquad \vec{P}_{T,h} \cdot \vec{P}_{T,i} < 0. \tag{8}$$

[4] In this paper, a "bin" refers to a kinematic domain in x and Q^2 for which one double differential cross-section measurement is made.

To identify the positron in NC events, the presence of a compact and isolated electromagnetic cluster of energy in the LAr calorimeter is required [38]. For $\theta_e > 35°$, the positron candidate is validated only if it is associated with a charged particle by requiring the distance of closest approach of an extrapolated track to be less than $12\ \mathrm{cm}$ from the cluster. Fiducial cuts are applied to ensure the quality of the positron reconstruction (section 2.6.2). Events are also not included if $\theta_e \gtrsim 153°$, because then the electromagnetic shower of the scattered positron is not fully contained in the LAr calorimeter. The measurements are thus restricted to $Q^2 \geq 150\ \mathrm{GeV}^2$. NC events with such an identified positron are required to satisfy the following cuts:

- cluster energy E'_e greater than $11\ \mathrm{GeV}$;
- inelasticity y_e lower than 0.9;
- $E-p_z$ (eq. 5) greater than $35\ \mathrm{GeV}$.

These requirements minimize the size of radiative corrections applied in the analysis (section 3.1) and reduce the background due to photoproduction.

After all the different steps of the event selection, and additional requirements described below to reject events from background processes, the DIS data sample comprises about $75\ 000$ NC events and 700 CC events.

2.5 Background Rejection

The CC and NC event samples which result from the selection procedures described above (section 2.4) contain both non-ep background arising from particles produced in proton-nucleus interactions and from cosmic rays, and ep-induced background.

2.5.1 Non-ep Background

Events resulting from processes other than ep collisions originate from cosmic rays, from "beam halo muons" of the proton beam which interact in the detector material and cause electromagnetic showers, and from protons interacting with residual particles in the beam pipe (beam-gas events) or with the beam pipe itself (beam-wall events).

A large fraction of these background events are removed by requiring that the event time T_0, determined from the drift times of hits from tracks in the CJC, is coincident with the collision time at the ep interaction region. In the CC analysis the background is further reduced by using in addition the T_0 determined from the rise times of signals in the LAr calorimeter.

The remaining background is found to be negligible in the NC sample. Further reductions are necessary in the CC analysis in which the background mainly originates from random coincidences between soft photoproduction events and cosmic rays or beam-halo muons. The majority of these events are rejected using topological requirements following reconstruction of a cosmic ray or a beam-halo muon using information from the LAr and SPACAL calorimeters, the CJC and the Instrumented Iron [11, 24, 39, 40].

The inefficiency in the CC selection introduced by these requirements is determined in two different ways. A visual scan of rejected events yields an overall inefficiency for the CC selection of $5 \pm 2\%$. This result is consistent with the inefficiency obtained when using NC events in which the presence of the scattered positron is ignored.

The residual contamination of non-ep induced background events in the CC sample is determined to be 3.7% by visual scanning. These events are then rejected so that the remaining uncertainty in the CC sample from non-ep background is below 0.5%.

2.5.2 ep-induced Background

The main ep-induced background in the CC sample originates from γp events and from NC events in which the scattered positron is not identified. Mismeasurement of energies and limited geometrical acceptance can in both cases lead to events which are not balanced in transverse momentum.

In CC events the energy flow is concentrated in the hemisphere opposite to the transverse momentum of the scattered neutrino, resulting in a low value for V_{ap}/V_p (eqs. 7, 8) while in γp and NC background events it is more isotropic, giving values of V_{ap}/V_p close to 0.5. This is seen in fig. 1a where the V_{ap}/V_p distribution is shown for γp events for which the scattered positron is measured in the electron tagger and which pass the CC selection, apart from the cut on V_{ap}/V_p. The observed distribution is well described in shape and normalization by the γp simulation. An error of $\pm 30\%$ on the simulation of the photoproduction background is shown on the figure.

The same distribution, shown in fig. 1b for all events that pass the CC selection apart from the cut on V_{ap}/V_p, is well described by the simulation of CC and background ($\mathrm{bg} \equiv \gamma p$ + NC) events. The cut of $V_{ap}/V_p < 0.15$, applied in the CC selection, rejects a large fraction of this background. According to the simulation, about 70% (95%) of the CC events with $12 < P_T^{\mathrm{miss}} < 15$ GeV ($P_T^{\mathrm{miss}} > 25$ GeV) survive this cut. To evaluate the systematic uncertainty

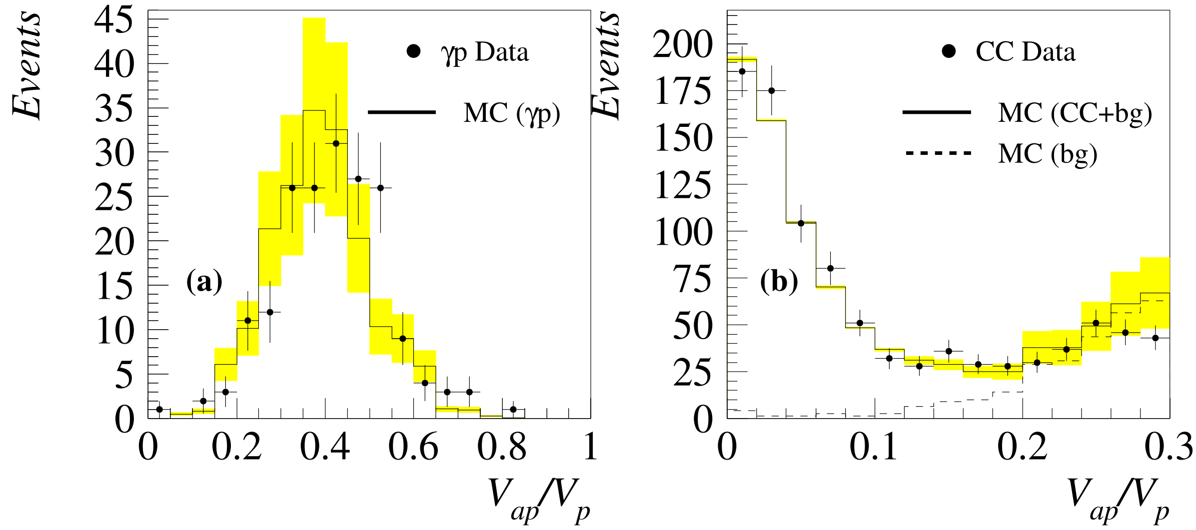

Figure 1: *(a) Distribution of V_{ap}/V_p for tagged γp events passing the CC selection except for the V_{ap}/V_p cut. The simulation (histogram) of the γp background normalized to the experimental luminosity is compared to the data. (b) Distribution of V_{ap}/V_p for the CC event sample. The simulation (histogram), which includes the CC and the background ($\mathrm{bg} \equiv \gamma p$ + NC) events, is normalized to the experimental luminosity and compared to the data. A cut $V_{ap}/V_p < 0.15$ is applied in the CC selection. The shaded error bands represent the systematic uncertainty of the background simulation.*

in the CC selection which is introduced by this requirement, the cut value of V_{ap}/V_p is varied between 0.13 and 0.17 in the simulation, keeping this value fixed for the data. A variation in the efficiency with which CC events are retained of 5% (2%) at low (high) $P_T^{\rm miss}$ is then observed. The resulting error on the cross-section measurement is 10% at low Q^2 and becomes negligible for $Q^2 > 1000\ \mathrm{GeV}^2$.

To reject residual background due to NC events in the CC sample, events with only one track with azimuthal angle opposite to the hadronic final state ($|\varphi_{track} - \varphi_h| > 160°$) are removed. The azimuthal angle φ_h of the hadronic final state is defined by $\tan \varphi_h = p_{y,h}/p_{x,h}$. Events with large $P_T^{\rm miss}$ and isolated high momentum leptons have been observed recently [41] and they are removed in this analysis by applying the selection procedure for such events which is used there. The additional inefficiency introduced into the CC selection due to these requirements is less than 1%.

The remaining contamination due to ep-induced background is evaluated from the simulation and statistically subtracted from the data. The background corresponds to about 10% at the lowest Q^2 values and less than 2% for $Q^2 > 1000\ \mathrm{GeV}^2$.

In the NC analysis, after all selection cuts, the only significant background is due to events from photoproduction processes in which the scattered positron escapes the detector along the beam pipe and one of the particles of the hadronic final state is misidentified as the scattered positron. As in the CC case, this background is determined from the simulation, controlled using the subsample of about 10% of the γp events in which the scattered positron is detected in the electron tagger, and subtracted from the data. It amounts to less than 1% in the total sample and to at most 5% in the highest y bins at Q^2 below $1000\ \mathrm{GeV}^2$.

Elastic QED-Compton events fulfill all the NC selection requirements. Such events, which represent less than 0.5% of the total sample are removed from the data sample based on their topological characteristics: they have two electromagnetic clusters, one reconstructed track and no hadronic activity in the calorimeters.

2.6 Detector Alignment and Calibration

At high Q^2, the scattered positron and the hadronic final state are predominantly measured with the LAr calorimeter. From test beam data, the initial electromagnetic and hadronic energy scales were established with an uncertainty of about 3% for electrons and pions of energy between $4\ \mathrm{GeV}$ and $205\ \mathrm{GeV}$ [42, 43]. These energy scales were verified *in situ* at HERA using the 1994 data [6]. The tracking detectors are used wherever possible to improve these measurements by making use of their good angular precision for the scattered positron, and of their good precision in both angle and momentum measurement to improve the determination of the hadronic final state energy. This section is concerned with the methods used to reconstruct the positron angle, the positron energy, and the hadronic energy.

2.6.1 Positron Angle Measurement

The polar angle of the scattered positron is determined using the central tracking detectors when its track is reconstructed using hits in the 3 central chambers CJC, CIZ and COZ. When the positron's track is less well constrained, the angle is determined from the position of the positron energy cluster in the LAr calorimeter and the vertex reconstructed using the charged tracks in the event.

By minimizing the spatial discrepancy between the positron track and the location of the calorimeter cluster, the alignment of the tracking detectors relative to the LAr calorimeter was established to within $1\ \mathrm{mm}$ in the x, y and z directions.

Following this alignment, the precision of the angle measurement with the tracking detectors (with the calorimeter cluster and event vertex) is better than $1\ \mathrm{mrad}$ ($3\ \mathrm{mrad}$). The proportion

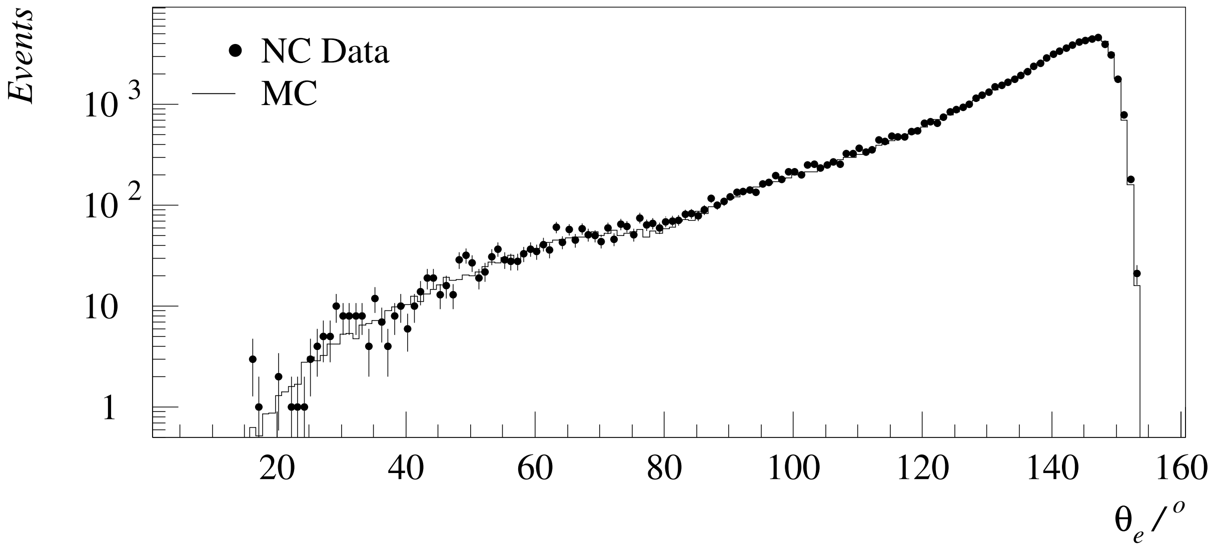

Figure 2: *Distribution of polar angle of the scattered positron: the histogram is from the Monte Carlo (MC) simulation.*

of scattered positrons in which θ_e is determined from the cluster and event vertex is about 40%. This proportion increases to 100% in the forward region, for $\theta_e < 35°$. The vertex is determined from the tracking detectors with a precision of approximately $3\ \mathrm{mm}$ in z and $1\ \mathrm{mm}$ in x and y. Because the means of the distribution of event vertices depend on the characteristics of the stored positron and proton beams, the vertex distribution is determined from the data for every beam storage, and in event simulation the vertex distribution is adjusted to follow these changes.

The θ_e distributions for the data and for the simulation are shown in fig. 2. The simulation describes the data well throughout the complete angular range.

2.6.2 Positron Energy Measurement

For the present cross-section analysis, the calibration constants and their uncertainties have been improved compared to the previous H1 measurements, making use of the increased NC event sample and exploiting the overconstrained kinematic reconstruction.

Before the *in situ* calibration discussed below, the measured positron energy is corrected for energy loss in the material in front of the calorimeter (between $0.7X_\circ$ and $2.5X_\circ$). Further energy loss can occur in the cracks between the calorimeter modules in the z and φ directions. To limit the size of the corrections which occur because of the crack regions, the impact position of the positron track on the calorimeter is required to lie outside a fiducial area of $\pm 2°$ around a φ crack and $\pm 5\ \mathrm{cm}$ around the $z-$crack located between the CB2 and CB3 wheels of the LAr

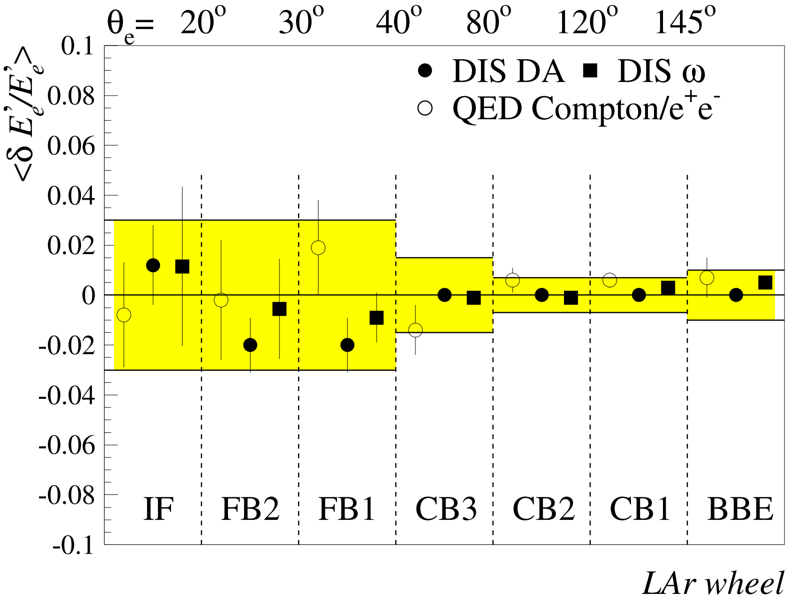

Figure 3: *Comparison of the electromagnetic energy scale as determined by different calibration methods. Shown is $\langle \delta E'_e / E'_e \rangle$, the mean fractional energy shift of the different methods from the absolute energy scale. The shaded error band shows the systematic uncertainty on the energy scale quoted on this measurement, which varies from 0.7% to 3%, depending on the position in the detector.*

calorimeter (see fig. 3 for the angular coordinates of the seven electromagnetic wheels of the LAr calorimeter) [21].

For the *in situ* calibration of the barrel region ($\theta_e > 40°$), only the NC events with $y_\Sigma < 0.3$ ($y_\Sigma < 0.5$) in the region of $80° \lesssim \theta_e \lesssim 153°$ ($40° \lesssim \theta_e \lesssim 80°$) are used. For these y values the energy of the scattered positron is predicted precisely by the double-angle (DA) method [44] in which the kinematic variables are determined solely from θ_e and γ_h. The calibration is achieved by constraining the mean of the $E'_e/E_{\rm DA}$ distribution to 1 via small local modifications of the calibration constants. These constants are determined for data and simulation separately in finely segmented z and φ regions defined by the impact position of the positron track on the LAr calorimeter. The calibration constants vary typically by $\pm 1\%$ around their average values, except in the regions affected by z-cracks, where the corrections may reach up to 8% [24]. Outside these regions, the difference between the calibrated energy response of the data and the simulated events is smaller than 0.5%. The absolute calibration is obtained by applying on data and simulation corrections of about 1%, derived from the simulation. These corrections take into account effects from initial state QED radiation and small biases originating from the imperfect γ_h reconstruction.

Due to the limited number of events with positrons in the forward region ($\theta_e < 40°$) two event samples, elastic QED Compton and exclusive two photon e^+e^- pair production, are used in addition to the DIS events. The requirement of transverse momentum balance, allows the energy of the more forward electromagnetic energy deposit to be determined from the well calibrated backward cluster. For the DIS events the ω method [45] is used to determine the calibration constants instead of the DA method since it is less sensitive to the effects of initial state

QED radiation and is therefore more reliable when there are low statistics. A single calibration constant is determined for the entire forward region.

After the application of these calibration procedures, the positron energy scale is checked using the elastic QED-Compton and e^+e^- event sample and, separately, the ω method for the DIS sample for each calorimeter wheel. The results, shown in fig. 3, from all the different methods are found to be in good agreement. An error of $\pm 0.7\%$ $(1.0\%, 1.5\%, 3.0\%)$ on the absolute electromagnetic energy scale of the CB1–CB2 (BBE, CB3, FB1–IF) wheels of the detector can therefore be assigned. The uncertainties in the electromagnetic energy scale increase towards the forward region due to the decreasing number of events. The resulting energy spectra are presented for $Q^2 > 150$ (5000) GeV^2 in fig. 4a(b), and are well described by the simulation within the normalization uncertainty of $\pm 1.5\%$.

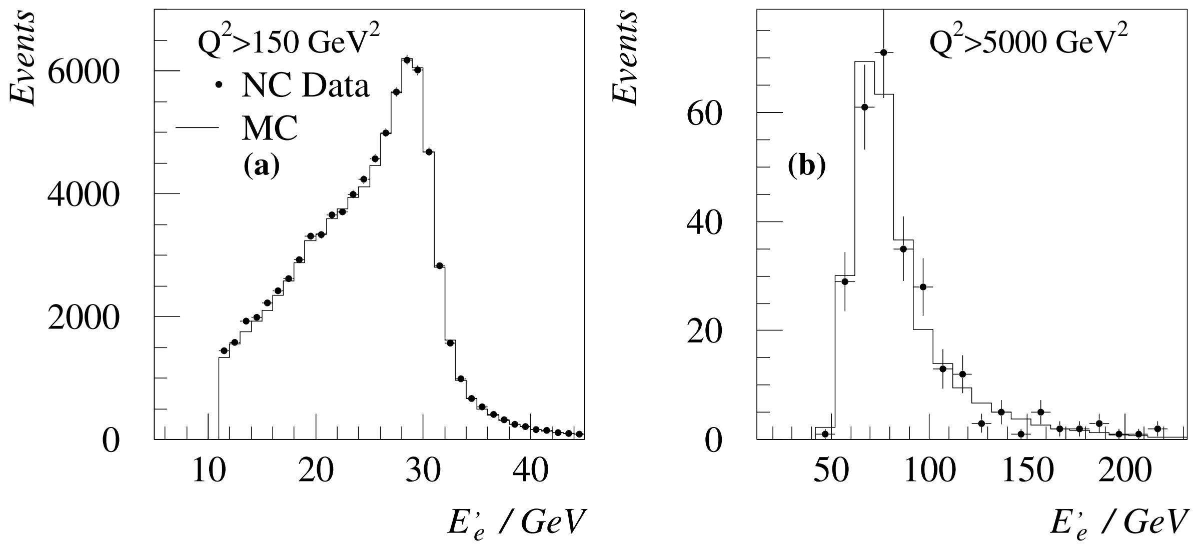

Figure 4: *(a) Energy spectrum of the scattered positron at* $Q^2 > 150$ GeV^2*, and (b)* $Q^2 > 5000$ GeV^2*. The simulation (histogram), which is normalized to the integrated* ep *luminosity of the data, is shown together with the data (points).*

2.6.3 Hadronic Energy Measurement

The optimal measurement of the hadronic final state energy is obtained after applying specific techniques to the reconstruction of the calorimeter and tracking information, as described in the following.

Since the H1 LAr calorimeter is non-compensating, weighting algorithms are applied to the hadronic clusters in order to improve the energy resolution [43, 46]. A further improvement in energy resolution of about 10 to 20% for events having a $P_{T,h}$ between 10 to 25 GeV is obtained by using a combination of the momentum of low transverse momentum particles ($P_T < 2$ GeV) measured in the central tracking detector with the energy deposited by other particles of the hadronic final state measured in the calorimeter. To avoid "double counting", the energy measured in the electromagnetic (hadronic) LAr calorimeter in a cylinder of $15(25)$ cm in radius around the axis given by the direction of a low transverse momentum track is not included, except if the total energy in the cylinders is greater than the energy of the track, in which case only the calorimetric measurement is used. The fraction of y_h measured by each of the subdetectors (LAr, tracks, SPACAL) is shown in fig. 5a to be well described by the simulation in the range $0.005 \leq y_h \leq 0.9$. The contribution of the SPACAL calorimeter is below 10% except at high y.

At low $y \lesssim 0.05$, where little energy is deposited in the calorimeter and hadrons are produced in the forward direction, the measurement of the kinematic variables is distorted by the presence of "noise" in the calorimeter cells due either to the electronics of the calorimeter readout, or to the secondary scattering of final state particles into the calorimeter. Both sources of noise are included in the simulation. The noise is reduced by suppressing isolated low energy deposits [47], which results in a significant improvement of the reconstruction of the kinematic variables at low y. The fraction of y_h identified as noise is shown in fig. 5a to be described by the simulation. The effect of a variation of $\pm 25\%$ of the subtracted noise contribution is included in the systematic error.

The *in situ* calibration of the hadronic energy scale is performed by comparing the transverse

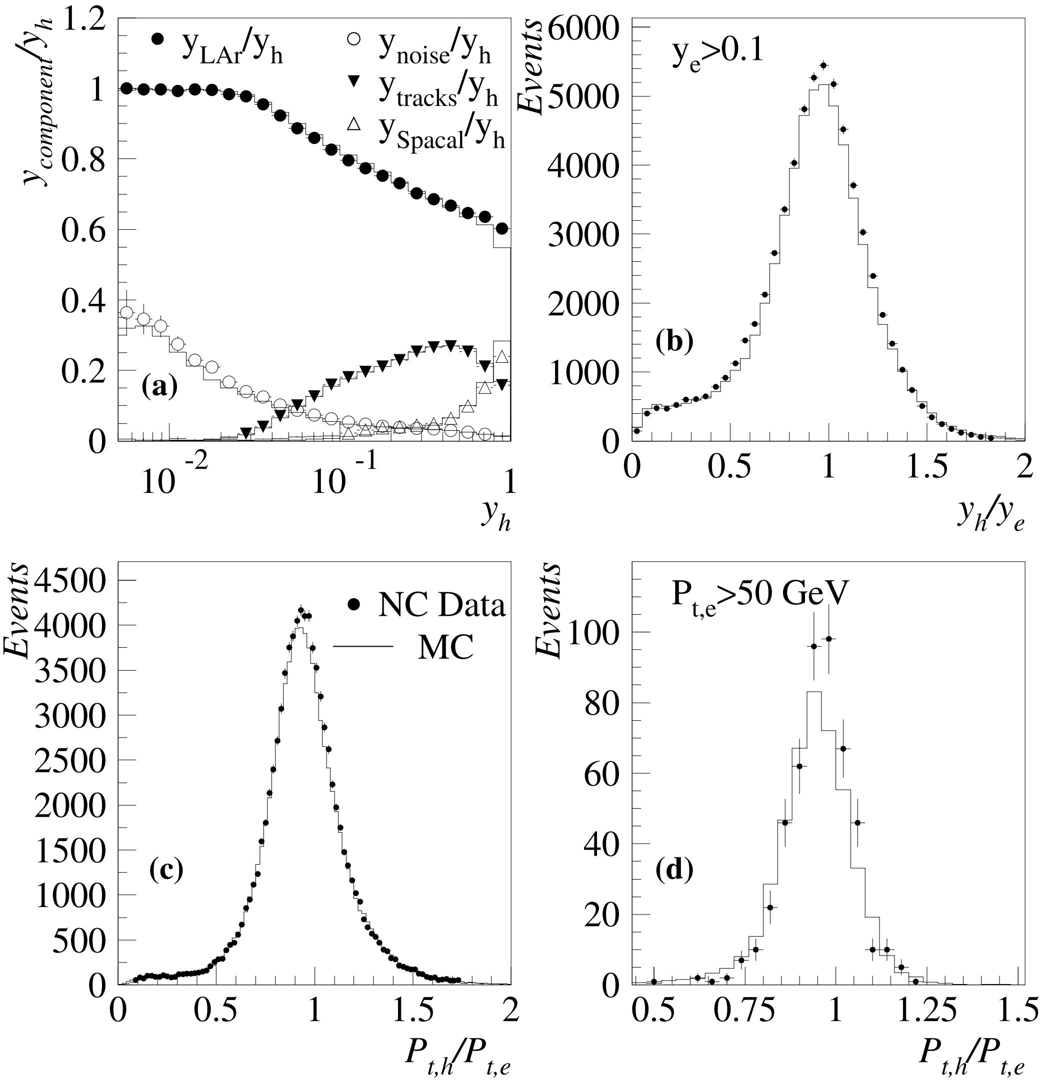

Figure 5: *(a) Distribution of the fraction of y_h contributed by the tracks (y_{tracks}), the LAr (y_{LAr}) and the SPACAL calorimeters (y_{Spacal}), and the fractional contribution of the subtracted noise (y_{noise}). (b) Distribution of y_h/y_e for $y_e > 0.1$. (c) Distribution of $P_{T,h}/P_{T,e}$ for the complete NC sample, (d) for the subsample at $P_{T,e} > 50$ GeV. The simulation (histogram) normalized to luminosity is compared to the data (points).*

momentum of the precisely calibrated positron (section 2.6.2 above) to that of the hadronic system in NC events. Calibration constants are determined for each of the 7 electromagnetic and 8 hadronic wheels. The calibration factor for each wheel is evaluated using the ratio $P_{T,h}/P_{T,e}$ of each event weighted with the fraction of $P_{T,h}$ carried by the wheel. The calibration constants are adjusted iteratively until the average ratio $\langle P_{T,h}/P_{T,e}\rangle$ is equal between the data and the simulation in all regions of the detector.

Detailed studies of the dependence of $P_{T,h}/P_{T,e}$ and y_h/y_e on P_T and γ_h justify a systematic error on the relative hadronic energy scale of the LAr calorimeter of 2% [48]. A further confirmation of this scale uncertainty is obtained when separating the NC sample in two: one with events with one well reconstructed jet, the other with a multijet topology. In the first subsample, the jet direction directly determines the wheel containing the maximum amount of transverse energy, and the corresponding wheel calibration constant could thus been checked precisely. In the multijet sample the $P_{T,h}/P_{T,e}$ distribution has also been observed to be better described by the simulation after applying the new hadronic calibration.

The dependence of the calibration on the usage of two different hadronic final state models in the simulation, one which uses the matrix elements plus parton shower model (MEPS) as implemented in LEPTO [28], the other one being the colour dipole model in its ARIADNE [29] implementation, has been studied and found to be negligible.

The resulting hadronic final state reconstruction is summarized in fig. 5b,c,d. In fig. 5b the y_h/y_e distribution for $y_e > 0.1$ is shown. In this distribution the hadronic energy enters with a different angular weight than in the $P_{T,h}/P_{T,e}$ distribution. The agreement observed between data and simulation shows that the hadronic calibration is valid for the energy itself, and not only for the transverse energy. Fig. 5c(d) shows the $P_{T,h}/P_{T,e}$ distribution in the complete NC event sample (with $P_{T,e} > 50$ GeV). In these two distributions, the data are described by the simulation within the quoted 2% uncertainty. More details on the calibration procedures can be found in [48].

3 Cross-Section Measurement Procedure

3.1 Cross-Sections and Structure Functions

In this section the cross-section definitions are introduced together with the procedure adopted for the treatment of radiative corrections. The measured cross-sections are:

- the NC(CC) double differential cross-section $d^2\sigma_{NC(CC)}/dxdQ^2$;
- the NC(CC) single differential cross-sections $d\sigma_{NC(CC)}/dQ^2$ and $d\sigma_{NC(CC)}/dx$.

These cross-sections are presented after corrections for the effects of QED radiation have been made. They are derived from the cross-sections (labeled $init$) which are determined using the measurement procedure described in section 3.3. Thus the double differential NC (CC) cross-sections are defined as

$$\frac{d^2\sigma_{NC(CC)}}{dx\;dQ^2} = \left(\frac{d^2\sigma_{NC(CC)}}{dx\;dQ^2}\right)_{init}\left[1+\delta^{qed}_{NC(CC)}(x,Q^2)\right]. \qquad (9)$$

The δ_{NC}^{qed} term includes the effects of photon emission from the lepton line, the effects of the photonic lepton vertex corrections combined with the self energies of the external fermion lines[5], and the effects of the fermion loops of the exchanged photon self energy. The δ_{CC}^{qed} term includes the leptonic part of the $\mathcal{O}(\alpha)$ photonic correction to CC processes [49, 50]. These radiative corrections are calculated using DJANGO [26] and verified with the HECTOR [51] program.The weak radiative corrections $\delta_{NC(CC)}^{weak}$ which are defined in [52] and which are small (of the order of 1%), have not been made on the measured cross-sections.

When extracting the structure functions of the proton from cross-section measurements, the weak radiative corrections are however applied. The Born cross-section is then defined as

$$\left(\frac{d^2\sigma_{NC(CC)}}{dx\ dQ^2}\right)_{Born} = \frac{d^2\sigma_{NC(CC)}}{dx\ dQ^2} \quad \left[1+\delta_{NC(CC)}^{weak}(x,Q^2)\right]. \tag{10}$$

The Born double differential NC cross-section for $e^+p \to e^+X$ can be written as

$$\left(\frac{d^2\sigma_{NC}}{dx\ dQ^2}\right)_{Born} = \frac{2\pi\alpha^2}{x}\left(\frac{1}{Q^2}\right)^2 \ \phi_{NC}(x,Q^2), \tag{11}$$

where

$$\phi_{NC}(x,Q^2) = Y_+\tilde{F}_2(x,Q^2) - Y_- x\tilde{F}_3(x,Q^2) - y^2\tilde{F}_L(x,Q^2). \tag{12}$$

Here α is the fine structure constant taken to be $\alpha \equiv \alpha(Q^2=0)$. The "structure function term" $\phi_{NC}(x,Q^2)$ is a linear combination of the $\tilde{F}_2$ structure function, the longitudinal structure function $\tilde{F}_L$, and the $x\tilde{F}_3$ structure function which in the Standard Model is significant only when Q^2 is sufficiently large to render Z° exchange non-negligible. The helicity dependences of the electroweak interactions are contained in the functions $Y_\pm = 1 \pm (1-y)^2$.

In leading order QCD, the structure function term is simply related to the sum of the u and d quark densities, weighted with the squared quark charges, when neglecting Z° exchange and the contribution of heavier quarks:

$$(\phi_{NC})_{LO} = \left[1+(1-y)^2\right] \ x \ \left[\frac{4}{9}(u+c+\bar{u}+\bar{c}) + \frac{1}{9}(d+s+\bar{d}+\bar{s})\right]. \tag{13}$$

At high x the structure function term ϕ_{NC} predominantly gives information on the valence distribution of the u quark.

For unpolarized beams, the structure functions $\tilde{F}_2$ and $x\tilde{F}_3$ can be decomposed, taking into account Z° exchange, as [53]

$$\tilde{F}_2 \equiv \ F_2 \ - v\frac{\kappa_w Q^2}{(Q^2+M_Z^2)} \ F_2^{\gamma Z} + (v^2+a^2)\left(\frac{\kappa_w Q^2}{Q^2+M_Z^2}\right)^2 F_2^Z \tag{14}$$

$$x\tilde{F}_3 \equiv \ - a\frac{\kappa_w Q^2}{(Q^2+M_Z^2)} xF_3^{\gamma Z} + \ (2va) \ \left(\frac{\kappa_w Q^2}{Q^2+M_Z^2}\right)^2 xF_3^Z, \tag{15}$$

where M_Z is the mass of the Z°, $\kappa_w = 1/(4\sin^2\theta_w\cos^2\theta_w)$ is a function of the Weinberg angle (θ_w), and v and a are the vector and axial couplings of the electron to the Z°. They are related

[5] The radiative corrections due to the exchange of two or more photons between the lepton and the quark lines are small and are included in the radiative correction systematic error.

to the weak isospin of the electron, namely $v = -\frac{1}{2} + 2\sin^2\theta_w$, and $a = -\frac{1}{2}$ [54]. The electromagnetic structure function F_2 originates from photon exchange only, and the functions F_2^Z (F_3^Z) and $F_2^{\gamma Z}$ ($F_3^{\gamma Z}$) are the contributions to $\tilde{F}_2(x\tilde{F}_3)$ due to Z° exchange and γZ° interference respectively. Note that for unpolarized beams, $\tilde{F}_2$ is the same for electron and for positron scattering, while the $x\tilde{F}_3$ term in eq. 12 changes sign.

The NC "reduced cross-section" is defined from the measured $d^2\sigma_{NC}/dxdQ^2$ mainly to reduce the Q^2 dependence on the propagator:

$$\tilde{\sigma}_{NC}(x,Q^2) \equiv \frac{1}{Y_+}\,\frac{Q^4\,x}{2\pi\alpha^2}\,\frac{d^2\sigma_{NC}}{dxdQ^2}. \tag{16}$$

In the major part of the (x, Q^2) domain, F_2 is the dominant component of the structure function term $\phi_{NC}(x, Q^2)$, and $\tilde{\sigma}_{NC}$ is conveniently expressed as

$$\tilde{\sigma}_{NC} \;=\; F_2\,(1 + \Delta_{F_2} + \Delta_{F_3} + \Delta_{F_L})\;/\;(1 + \delta_{NC}^{weak}) \;=\; F_2\,(1 + \Delta_{all}), \tag{17}$$

with the Δ_{F_2} and Δ_{F_3} terms originating from the $F_2^{\gamma Z}$, F_2^Z and $F_3^{\gamma Z}$, F_3^Z functions defined in eq. 14 and 15, and the Δ_{F_L} term from the longitudinal structure function. These terms, as obtained from the NLO QCD Fit described in section 3.2, are given in table 4.

In the kinematic range investigated the effect of Z° exchange ($\Delta_{F_2} + \Delta_{F_3}$) on $\tilde{\sigma}_{NC}$ are expected to be $\leq\ 5\%$ for $Q^2 < 5000\ \mathrm{GeV}^2$ (table 4). It is thus possible to extract F_2 with little uncertainty from the measured cross-section for values of Q^2 below $5000\ \mathrm{GeV}^2$. At higher Q^2 values the contribution of the $x\tilde{F}_3$ term significantly reduces the e^+p cross-section, and the determination of F_2 then relies strongly on the calculation of Δ_{F_2} and Δ_{F_3}. In QCD calculations the Δ_{F_L} term is small and decreases at constant y with increasing Q^2. It reaches 6% for $y \geq 0.65$ and $Q^2 \leq 1500\ \mathrm{GeV}^2$ but is negligible for $y \lesssim 0.4$.

The Born double differential CC cross-section for $e^+p \to \bar{\nu}X$ can be written as

$$\left(\frac{d^2\sigma_{CC}}{dx\;dQ^2}\right)_{Born} = \frac{G_F^2}{2\pi x}\left(\frac{M_W^2}{M_W^2+Q^2}\right)^2 \phi_{CC}(x,Q^2), \tag{18}$$

where G_F is the Fermi coupling constant and the structure function term $\phi_{CC}(x, Q^2)$ can be decomposed into structure functions in a similar way as $\phi_{NC}(x, Q^2)$ [55].

For CC interactions a reduced cross-section

$$\tilde{\sigma}_{CC}(x,Q^2) \equiv \frac{2\pi x}{G_F^2}\left(\frac{M_W^2+Q^2}{M_W^2}\right)^2 \frac{d^2\sigma_{CC}}{dxdQ^2} \tag{19}$$

is also introduced, and is directly related to the CC structure function term by

$$\phi_{CC}(x,Q^2) = \tilde{\sigma}_{CC}(x,Q^2)\;\left[1 + \delta_{CC}^{weak}(x,Q^2)\right]. \tag{20}$$

In leading order QCD, neglecting the effect of quark mixing and the contribution of heavier quarks, the CC structure function term is related to the quark densities:

$$(\phi_{CC})_{LO} = x\;\left[(\bar{u}+\bar{c}) + (1-y)^2(d+s)\right]. \tag{21}$$

At high x the structure function term ϕ_{CC} predominantly gives information on the valence distribution of the d quark.

3.2 QCD Analysis Procedure

Comparison of the Standard Model with the measurements of the NC and CC ep cross-sections depends both on the model's explicit predictions for the interaction of a positron with a quark and the partonic content of the proton. The parameters of the electroweak theory, that describes quark-positron scattering in the Standard Model, have been measured precisely and are therefore fixed to their world average values [54] in this comparison. The parton distribution functions (PDFs), that describe the partonic structure of the proton, are not predicted by QCD and so must be obtained from the data. In order to obtain the PDFs together with their uncertainties, two NLO QCD fits are performed.

- The first fit (Low Q^2 Fit) is made with published low Q^2 DIS data: the proton (F_2) and deuteron (F_2^d) data from the BCDMS [4] and NMC [5] experiments are used, together with the 1994 F_2 measurements of H1 [6] at $Q^2 < 150\ \mathrm{GeV}^2$.

- The second fit (NLO QCD Fit) includes the high Q^2 NC and CC double differential cross-sections presented in this paper in addition to the datasets used in the Low Q^2 Fit. The results of this fit are presented in section 4.1.

Since the emphasis of this study is on the new data entering the fit which are at high Q^2, far above the squared masses of the charm (c) and bottom (b) quark, an approach is used in which all quarks are taken to be massless within the DGLAP equations and a cut of $Q^2 > 10\ \mathrm{GeV}^2$ is applied on the datasets. At high x and low W^2 ($W^2 \equiv Q^2(1-x)/x$) non-perturbative effects may have a large influence, therefore only the data having $W^2 \geq 20\ \mathrm{GeV}^2$ and $x < 0.7$ are used in the fits. The fixed target data are corrected for target mass effects using the Georgi-Politzer approach [56] and for deuteron binding effects using the method of [57] as constrained by SLAC measurements [58]. The effect of the deuteron corrections on the fit result are negligible for NC and up to 7% for CC at $x = 0.4$.

For these fits, the DGLAP evolution equations [10] are solved in the NLO $\overline{MS}$ factorization scheme using the QCDNUM program [59]. The results obtained have been cross-checked using an independent program [60]. A starting scale of $Q_0^2 = 4\ \mathrm{GeV}^2$ is taken at which four PDFs are parameterized. These are the u and d valence quarks (xu_v and xd_v), the gluon (xg), and the sea quark densities ($xS \equiv 2x[\bar{u} + \bar{d} + \bar{s} + \bar{c}]$). An asymmetry between the $\bar{d}$ and $\bar{u}$ PDFs is enforced by using the $\bar{d} - \bar{u}$ parameterization from [61] taking into account the different Q_0^2. The strange (s) quark density is constrained to be $\bar{s} = \bar{u}/2$ at Q_0^2 [62]. The charm component is normalized to 2% of the sea quark density at Q_0^2 since this gives a good description of the H1 measurements [63] of the charm induced structure function F_2^c . The xb density is evolved according to the DGLAP equations assuming that $b(x, Q^2) = 0$ for $Q^2 < 25\ \mathrm{GeV}^2$.

The functional forms of the parton densities are parameterized as:

$$xu_v(x, Q_0^2) = A_{u_v} x^{B_{u_v}} (1-x)^{C_{u_v}} (1 + D_{u_v} x^{E_{u_v}}) \quad (22)$$

$$xd_v(x, Q_0^2) = A_{d_v} x^{B_{d_v}} (1-x)^{C_{d_v}} (1 + D_{d_v} x^{E_{d_v}}) \quad (23)$$

$$xS(x, Q_0^2) = A_S x^{B_S} (1-x)^{C_S} \quad (24)$$

$$xg(x, Q_0^2) = A_g x^{B_g} (1-x)^{C_g}. \quad (25)$$

The parameters A_{u_v} and A_{d_v} are determined by enforcing the valence counting rules which require $\int_0^1 u_v dx = 2$ and $\int_0^1 d_v dx = 1$. The momentum sum rule allows the determination of one further normalization parameter, taken to be A_g. The strong coupling constant α_s is evolved according to QCD with the constraint $\alpha_s(M_Z^2) = 0.118$.

The fits are performed using the MINUIT program [65] which minimizes the χ^2 defined from the data value ($f_{i,j}^{data}$) and the theoretical expectation ($f_{i,j}^{theo}$) of the measured point i in the dataset j, normalized by the quadratic sum of its statistical ($\delta f_{i,j}^{sta}$) and uncorrelated systematic error ($\delta f_{i,j}^{unc}$):

$$\chi^2 = \sum_{j=1}^{N_{dataset}} \left[\sum_{i=1}^{N_j^{data}} \left(\frac{f_{i,j}^{data} \times (1 + \delta\mathcal{L}_j/\mathcal{L}_j) - f_{i,j}^{theo}}{\delta f_{i,j}^{sta} \oplus \delta f_{i,j}^{unc}} \right)^2 + \left(\frac{\delta\mathcal{L}_j}{\delta\mathcal{L}_j^0} \right)^2 \right]. \tag{26}$$

The number of datasets and data points in a dataset j are defined here as $N_{dataset}$ and N_j^{data}. The terms $(1 + \delta\mathcal{L}_j/\mathcal{L}_j)$ and $\delta\mathcal{L}_j^0/\mathcal{L}_j$ are respectively the normalization and the luminosity uncertainty of the dataset j. The normalizations of all datasets are allowed in this way to vary according to their quoted luminosity uncertainty (1.5% for the high Q^2 data, 1.5% for the H1 1994 data, 3% for BCDMS, 2.5% for NMC).

The results of the Low Q^2 Fit are presented in table 1 in which the χ^2 is given for each different dataset, together with their optimal relative normalization, according to the criteria discussed above. The total χ^2 per degree of freedom (ndf) is $548/(529 - 13) = 1.06$ when considering the uncorrelated error of the data (obtained from the quadratic sum of the statistical and systematic errors which are uncorrelated from one bin to another) as given in eq. 26. If the χ^2/ndf is recalculated using the total error of the data (obtained by adding the bin to bin correlated systematic error in quadrature to the uncorrelated error) its value decreases to 0.78.

Experiment	H1 94	BCDMS-p	BCDMS-D	NMC-p	NMC-D	Total
data points	77	139	133	90	90	529
χ^2 (unc. err.)	67	102	111	143	125	548
χ^2 (total err.)	39	89	98	93	77	396
normalization	1.01	0.97	0.98	0.99	0.99	

Table 1: *Results of the Low Q^2 Fit: for each experiment the following quantities are given: the number of data points, the contribution to the χ^2 using the uncorrelated error of the data (unc. err.) as obtained from the statistical and uncorrelated systematic error added in quadrature, the contribution to the χ^2 using the total error and the optimal normalization according to the fit.*

The uncertainty on the Standard Model expectations used to interpret the data in section 4 is estimated accounting for the experimental errors on the data points and by varying the theoretical assumptions of the QCD fit.

The “experimental error of the fit” is obtained by adding in quadrature the error from the QCD fit (performed with uncorrelated errors), to the contributions due to each bin to bin correlated systematic errors on the measurement. These correlated systematic errors are taken into account by repeating the QCD fit after varying the data points coherently under the influence of each error source separately.

The “theoretical error of the fit” is obtained by repeating the QCD fit after varying each of the fit assumptions in turn: the value of $\alpha_s(M_z)$ is varied by ± 0.003; the $s/\bar{s}$ contribution is changed by $\pm 25\%$; the $c/\bar{c}$ contribution at the starting scale is multiplied by a factor of 2; an uncertainty of $\pm50\%$ of the deuteron binding corrections is considered; the treatment of the $\bar{d}/\bar{u}$ asymmetry is changed to that given in [64] taking into account the different starting scale; the Q^2 cut applied to the data is raised to $15\ \mathrm{GeV}^2$. All the resulting differences with respect to the nominal fit, are added in quadrature to form an estimate of the theoretical error of the fit.

The "total error of the fit" is obtained by summing in quadrature these experimental and theoretical errors and is taken as the uncertainty on the Standard Model expectations. This procedure is also used in the determination of the QCD uncertainty for the fit of the CC cross-section to extract the W boson mass as described in section 4.8.

3.3 Experimental Procedure for the Cross-Section Measurement

The cross-sections are evaluated from the NC and CC DIS events, that pass the selection criteria described in section 2.4, by dividing the data into bins in the (x, Q^2) plane and correcting for acceptance and bin to bin migrations with the simulation. The simulation is found to reproduce the efficiencies of the selection cuts within the errors described in section 3.4. Where there are small discrepancies between data and simulation the efficiency of the simulation is adjusted to that of the data. The bin averaged cross-sections are converted to a cross-section at a chosen bin centre using a correction obtained from the NLO QCD Fit described in section 3.2.

The NC data are binned in Q^2 with 10 bins per order of magnitude, except at $Q^2 \geq 3000\ \mathrm{GeV}^2$, for which a binning twice as large is adopted to account for the rapidly decreasing number of events. The data are binned in x with 5 bins per order of magnitude, except at $x > 0.13$ and $Q^2 \leq 400\ \mathrm{GeV}^2$, for which a coarser binning is chosen to accommodate the degradation of the x resolution at very low y (< 0.02). The CC data are binned with 3 bins per order of magnitude in both Q^2 and x. The coarser CC binning is due to the smaller statistics of the CC sample and the inferior kinematic reconstruction resolution of the h method compared with the $e\Sigma$ method used for NC events. The bins which are used in this measurement have to satisfy two quality criteria which have been studied with the simulation: their stability and purity[6] are required to be larger than 30%.

The reliability of the cross-section measurements are checked by comparing the results obtained from different kinematic reconstruction methods. Fig. 6a shows that there is good agreement between the measurements of $\tilde{\sigma}_{NC}$ with the e and the $e\Sigma$ methods in the region where the e method is precise ($y \gtrsim 0.1$). Good agreement is also found between the $e\Sigma$, the Σ and the DA methods (not shown) over the whole y range. Fig. 6b shows the NC reduced cross-section in the CC binning, measured using the h and e methods. The good agreement between these two independent kinematic reconstruction methods demonstrates the reliability of the h method in the CC analysis.

3.4 Systematic Errors on the Cross-Section Measurement

The uncertainties on the measurement lead to systematic errors on the cross-sections which can be bin to bin correlated, or uncorrelated. All the correlated systematic errors have been checked to be symmetric to a good approximation and are assumed so in the following[7]. The correlated

[6] The stability (purity) is defined as the number of simulated events which originate from a bin and which are reconstructed in it, divided by the number of generated (reconstructed) events in that bin.

[7] For instance the effect of a $+0.5\%$ shift in the positron energy gives a systematic shift on the cross-section which is opposite to the effect of a -0.5% shift.

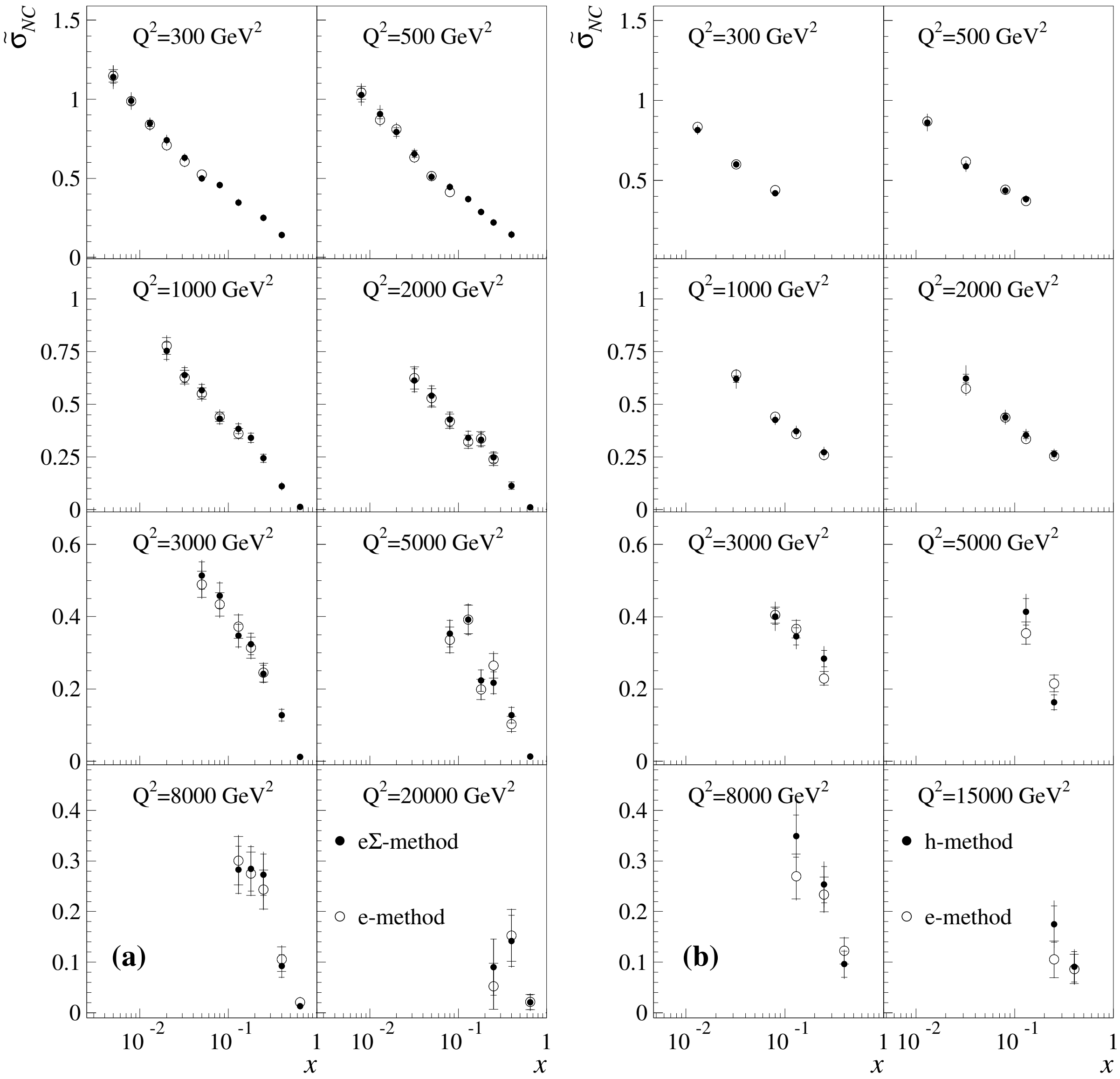

Figure 6: *Comparison of the NC reduced cross-section (as defined in eq. 16) measured (a) in the NC binning at eight different Q^2 values, with the e and eΣ method, and (b) in the CC binning with the e and the h method.*

systematic errors and the main uncorrelated systematic errors of the NC and CC cross-section measurements are given in table 8 and 9 and their origin is discussed below.

- An uncertainty of the positron energy of 1% if the z position of its impact on the calorimeter is in the backward part ($z < -145$ cm), 0.7% in the CB1 and CB2 wheels (-145 cm $< z < 20$ cm), 1.5% for 20 cm $< z < 100$ cm and 3% in the forward part ($z > 100$ cm). These uncertainties are obtained by the quadratic sum of an uncorrelated uncertainty and a bin to bin correlated uncertainty. This correlated uncertainty comes mainly from the potential bias of the calibration method and is estimated to be 0.5% in the whole LAr calorimeter. The resulting correlated (uncorrelated) systematic error on the NC cross-section is $\lesssim 3(5)\%$ except at the two highest x values.

- A correlated uncertainty of 1 mrad on the positron polar angle, and an uncorrelated uncertainty of 2 mrad. The uncorrelated uncertainty is the average of the different uncertainties when using the tracking system or the cluster for the polar angle determination. The resulting correlated (uncorrelated) systematic error is small, typically $\lesssim 1(2)\%$.

- A 2% uncertainty on the hadronic energy in the LAr calorimeter which is obtained from the quadratic sum of an uncorrelated systematic uncertainty of 1.7% and a correlated uncertainty of 1% originating from the calibration method and from the uncertainty of the reference scale ($P_{T,e}$). The resulting correlated systematic error increases at low y, and is typically $\lesssim 4\%$, except at high Q^2 for the CC measurements.

- A 7% (3%) uncertainty on the energy of the hadronic final state measured in the SPACAL (tracking system). Their influence on the cross-section is small compared to the uncorrelated uncertainty of the LAr calorimeter energy, and so the three contributions (LAr, SPACAL, tracks) have been added quadratically, giving rise to the uncorrelated hadronic error.

- A correlated 25% uncertainty on the energy identified as noise in the LAr calorimeter. The resulting systematic error is largest at low y, reaching $10 - 15\%$ at $x = 0.65$ and $Q^2 \leq 2000\ \mathrm{GeV}^2$ in the NC measurements.

- A 4 to 6% uncertainty on the efficiency of the V_{ap}/V_p cut at low $p_{T,h}$. The resulting correlated systematic error reaches values of about 12% in the CC analysis.

- A 30% uncertainty on the subtracted photoproduction background. The resulting correlated systematic error is always smaller than 5% in the NC and CC analysis.

The following uncertainties give rise to uncorrelated systematic errors on the cross-sections.

- A 2% error (4% at $y > 0.5$ and $Q^2 < 500\ \mathrm{GeV}^2$) from the positron identification efficiency in the NC analysis.

- A 1% error from the efficiency of the track-cluster link requirement in the NC analysis.

- A $0.5\%(2$ to $8\%)$ error from the trigger efficiency in the NC(CC) analysis.

- A $1\%(3\%)$ error from the QED radiative corrections in the NC(CC) analysis.

- A 3% error from the efficiency of the non-ep background finders, in the CC analysis.

- A 2% error (5% for $y < 0.1$) from the vertex finding efficiency in the CC analysis.

Overall the typical total systematic error for the NC (CC) double differential cross-section is about 5% (12%). For the $d\sigma/dQ^2$ measurements, the corresponding error is typically 3% (8%), see tables 6 and 7. In addition, a 1.5% normalization error, due to the luminosity uncertainty averaged over the years, has to be considered, but has not been added in the systematic error of the measurements given in the tables, or shown in the figures.

4 Results and Interpretation

4.1 Measurement of the NC Cross-Section $d^2\sigma_{NC}/dxdQ^2$

The NC reduced cross-section (eq. 16) is shown in fig. 7 as a function of x for fixed Q^2 values and listed in table 4. The measurement covers the range in y between 0.007 and 0.88. At $Q^2 \lesssim 500\ \mathrm{GeV}^2$ the total error is dominated by the systematic uncertainties in the energy scale and identification efficiency of the scattered positron and by the uncertainty in the energy scale of the hadronic final state. In this region the systematic error is typically 4%. At higher Q^2 the statistical error becomes increasingly dominant.

The kinematic domain of the NC cross-section measurements is significantly extended compared to previous HERA measurements both in Q^2 (from 5000 to $30\,000\ \mathrm{GeV}^2$) and towards higher x, with measurements at $x = 0.65$ for Q^2 between 650 and $20\,000\ \mathrm{GeV}^2$. The reduced cross-section rises steeply with decreasing x, corresponding to the increase of the sea-quark and gluon densities at low x. A sharp decrease of the cross-section at high x is also observed, as expected.

The NLO QCD Fit, described in section 3.2, is compared with the data in fig. 7. It provides a good description of the new measurements throughout the kinematic plane. The fit results in a value of $\chi^2/\mathrm{ndf} = 1.02$ for a total number of data points (ndp) of 684, when considering the uncorrelated error. If the total errors are used to determine the χ^2 a value of $\chi^2/\mathrm{ndf} = 0.77$ is obtained. The χ^2 values for each datasets of the NLO QCD Fit are given in table 2. The χ^2/ndp of the new high Q^2 (NC+CC) datasets is $(114 + 19)/(130 + 25) = 0.86$. The normalizations $(1 + \delta\mathcal{L}_j/\mathcal{L}_j)$ obtained by the fit for the different datasets are also given in the table. All datasets agree within 2% with their nominal normalization, with the exception of BCDMS-p which, however, has a luminosity error of 3%. The parameters of the NLO QCD Fit are given in table 3.

Experiment	H1 NC	H1 CC	H1 94	BCDMS-p	BCDMS-D	NMC-p	NMC-D	Total
data points	130	25	77	139	133	90	90	684
χ^2 (unc. err.)	114	19	65	112	104	143	126	683
χ^2 (total err.)	99	18	38	91	98	93	77	514
normalization	0.98	0.98	1.02	0.96	0.98	0.98	0.98	

Table 2: *Results on the NLO QCD Fit: for each experiment the following quantities are given: number of data points, contribution to the χ^2 using the uncorrelated error (unc. err.) as obtained from the statistical and uncorrelated systematic error added in quadrature, contribution to the χ^2 using the total error and the normalization required by the fit.*

The Low Q^2 Fit, described in section 3.2, is also compared with the data in fig. 7. The high Q^2 data agree well with the prediction. The fact that the new data are used in the NLO QCD Fit, results in a cross-section that is higher by a maximum of 2% at low x and is lower by a maximum of 3% at high x. These differences are, however, smaller than the uncertainty of the fit. At $Q^2 \approx 10\,000\ \mathrm{GeV}^2$ this uncertainty is reduced from 7 to 6% when including the high Q^2 data in the QCD fit.

In fig. 8 the reduced cross-section is shown as a function of Q^2 at fixed values of x for $0.08 \leq x \leq 0.65$. It can be seen that the H1 data are consistent with the fixed target data, in

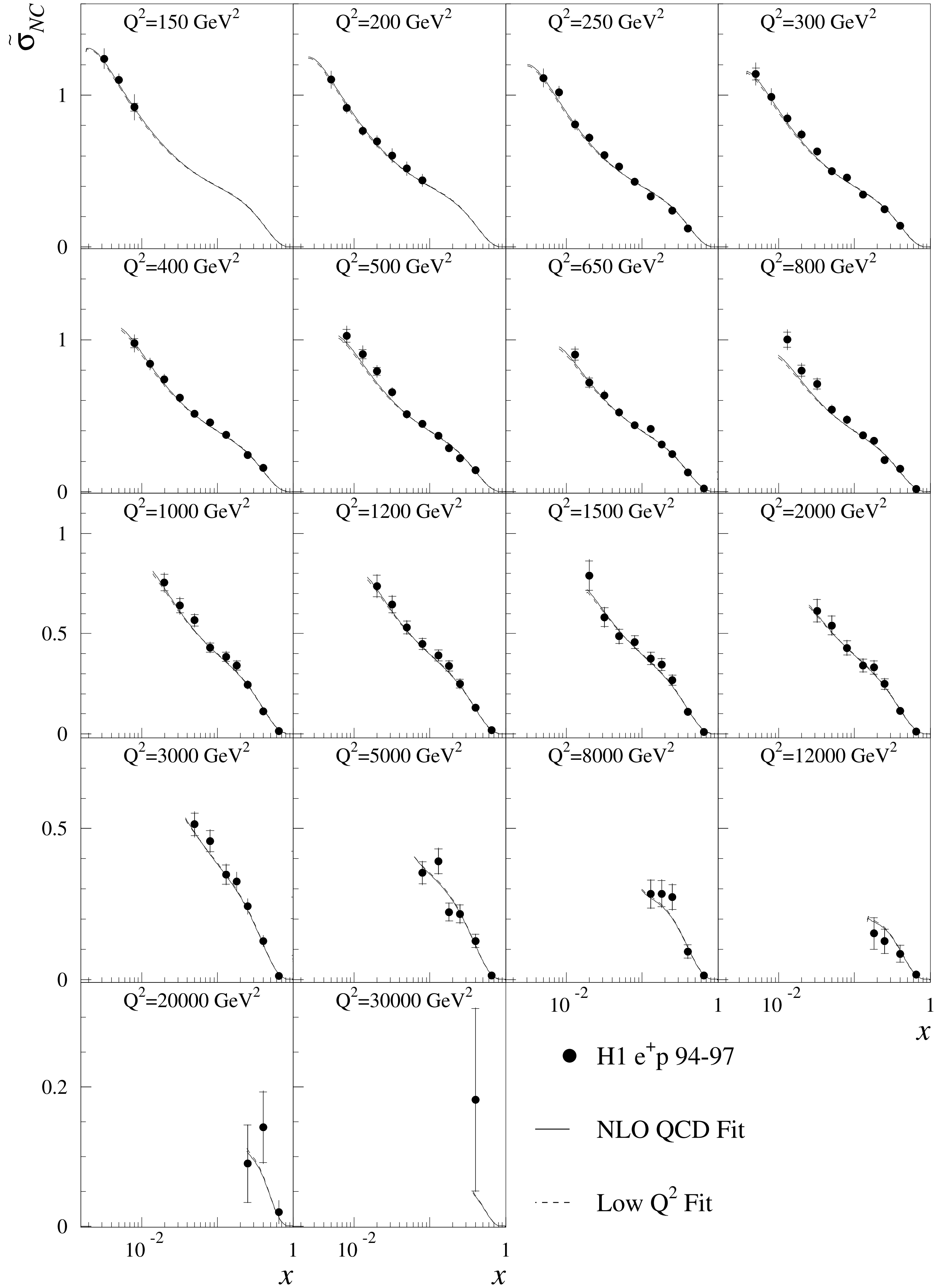

Figure 7: *NC reduced cross-section (as defined in eq. 16) as a function of x for different values of Q^2 compared with the NLO QCD Fit described in section 3.2. Also shown is the low Q^2 Fit. The inner error bars represent the statistical errors, the outer ones correspond to the total error.*

PDF	A_{PDF}	B_{PDF}	C_{PDF}	D_{PDF}	E_{PDF}
u_v	3.49	0.673	3.67	1.24	0.921
d_v	1.04	0.763	4.09	1.43	−0.067
S	0.69	−0.185	6.04		
g	2.64	−0.095	7.18		

Table 3: *Parameters of the NLO QCD Fit. The parameters A_g, A_{u_v}, and A_{d_v} are obtained from the sum rules. The parameters B_{u_v} and B_{d_v} are fixed (section 3.2).*

particular at $x = 0.25, 0.40$ in which the measurements are performed in contiguous kinematic regions. These measurements constrain the QCD evolution at high Q^2, and render possible the study of the structure function scaling violations at high x, in a region where non-perturbative effects are negligible.

At $x = 0.40$ an enhancement of the cross-section above the Standard Model expectation, as given by the NLO QCD Fit, is visible for the highest Q^2 values ($Q^2 > 15\,000\ \mathrm{GeV}^2$), which corresponds to the accumulation of events around an inclusive invariant mass of the lepton quark system of about $200\ \mathrm{GeV}$, as was already reported with the 1994–1996 data [13]. The significance of this excess decreases when 1997 data are included. A detailed analysis of these events is presented in [15].

At $x = 0.65$ and for $Q^2 < 10\,000\ \mathrm{GeV}^2$ the NLO QCD Fit lies above the H1 data. This difference can be due either to a high expectation at $x = 0.65$ since the main constraint on the fit comes from the BCDMS data which are known to favour a lower α_s value than the world average, or to the H1 data which share a correlated error of about 12% at this x value (table 8). The significance of this difference is reduced by the 7% uncertainty on the cross-section expectation (section 3.2).

The γZ° interference in e^+p collision is expected in the Standard Model to produce a decrease of the cross-section at $Q^2 \gtrsim M_Z^2 \approx 8000\ \mathrm{GeV}^2$. Such a reduction is observed with the highest Q^2 measurements, for $0.08 \leq x \leq 0.25$ as shown in fig. 8. To determine the extent to which Z^0 exchange is seen in the NC data, the NLO QCD Fit is repeated but allowing only for pure photon exchange (γ-exchange fit), i.e. $\tilde{F}_3 \equiv 0$ and $\tilde{F}_2 = F_2$. The γ-exchange fit, also shown in fig. 8, is observed to have a larger χ^2 than the standard NLO QCD Fit by 14.3 units, 11 of which are from the NC data at $Q^2 \geq 5000\ \ \mathrm{GeV}^2$. The description and χ^2 contributions of all other data is unchanged thereby showing that the effects of the γZ° interference are visible in DIS ep scattering at high values of Q^2.

4.2 Extraction of the Proton Structure Function $F_2(x, Q^2)$ at High Q^2

Assuming the validity of the electroweak sector of the Standard Model, and of the DGLAP equations at high Q^2, the electromagnetic proton structure function F_2 is extracted from the double differential NC cross-section (eqs. 12,14) using the NLO QCD Fit calculations for Δ_{F_L}, Δ_{F_2}, Δ_{F_3} and δ_{NC}^{weak}.

A comparison of the F_2 data at high Q^2 with the corresponding H1 [6] and ZEUS [7] results based on the 1994 data is shown in fig. 9. Only the data at Q^2 values which were measured in 1994 are shown here. The complete set of F_2 values is listed in table 4. The extension in kinematic coverage at low y (high x) is visible. A reduction of the systematic error of the new

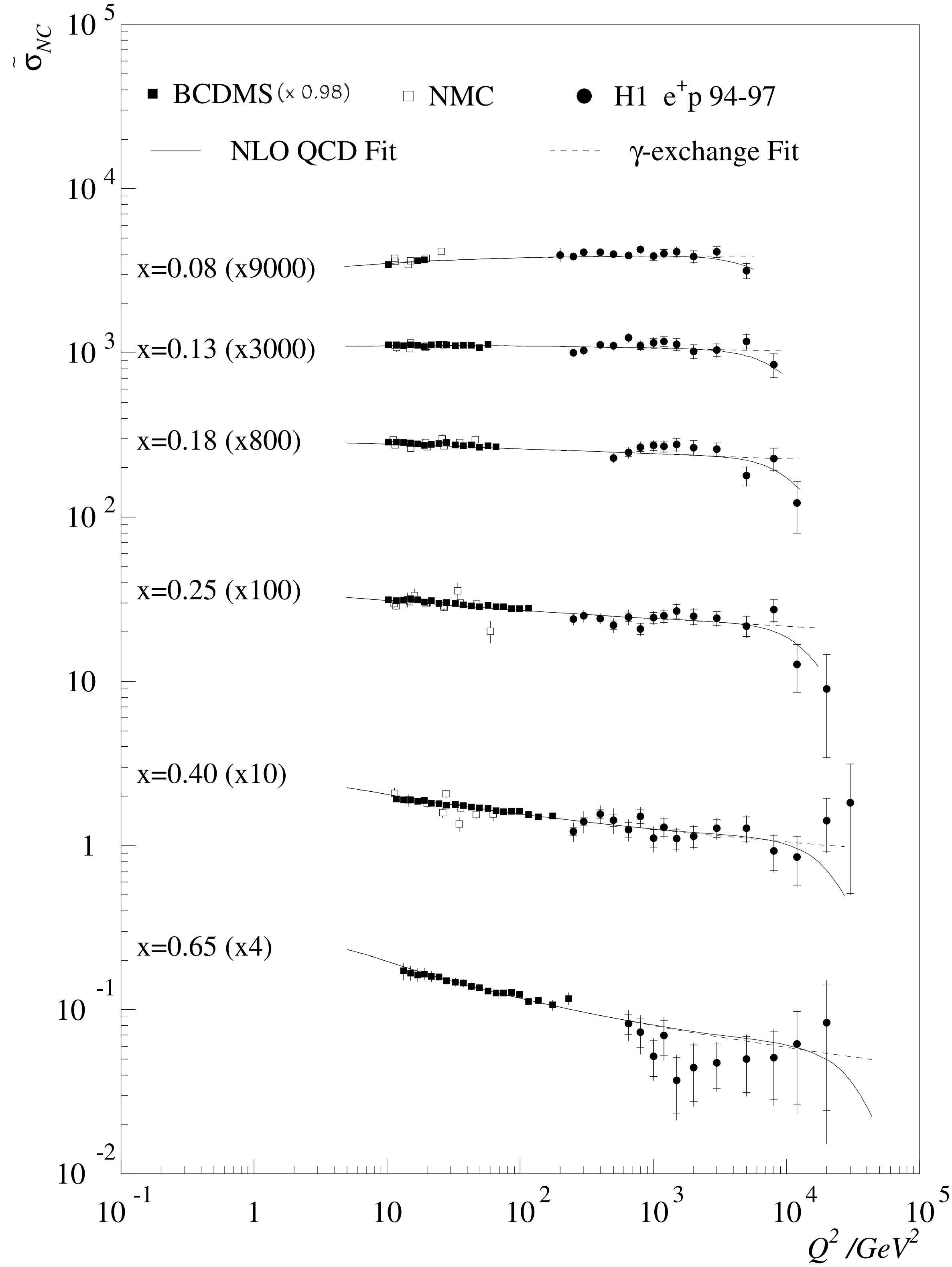

Figure 8: *NC reduced cross-section (as defined in eq. 16, solid points) at high x compared with Standard Model expectations as given by the NLO QCD Fit and with the γ-exchange fit (dashed line). The inner (outer) error bars represent the statistical (total) errors of the measurements. Also shown are the NMC data (open squares), and the BCDMS data (solid squares) which have been rescaled by -2%, as required by the normalization difference found by the QCD fit (table 2) between BCDMS and the high Q^2 data.*

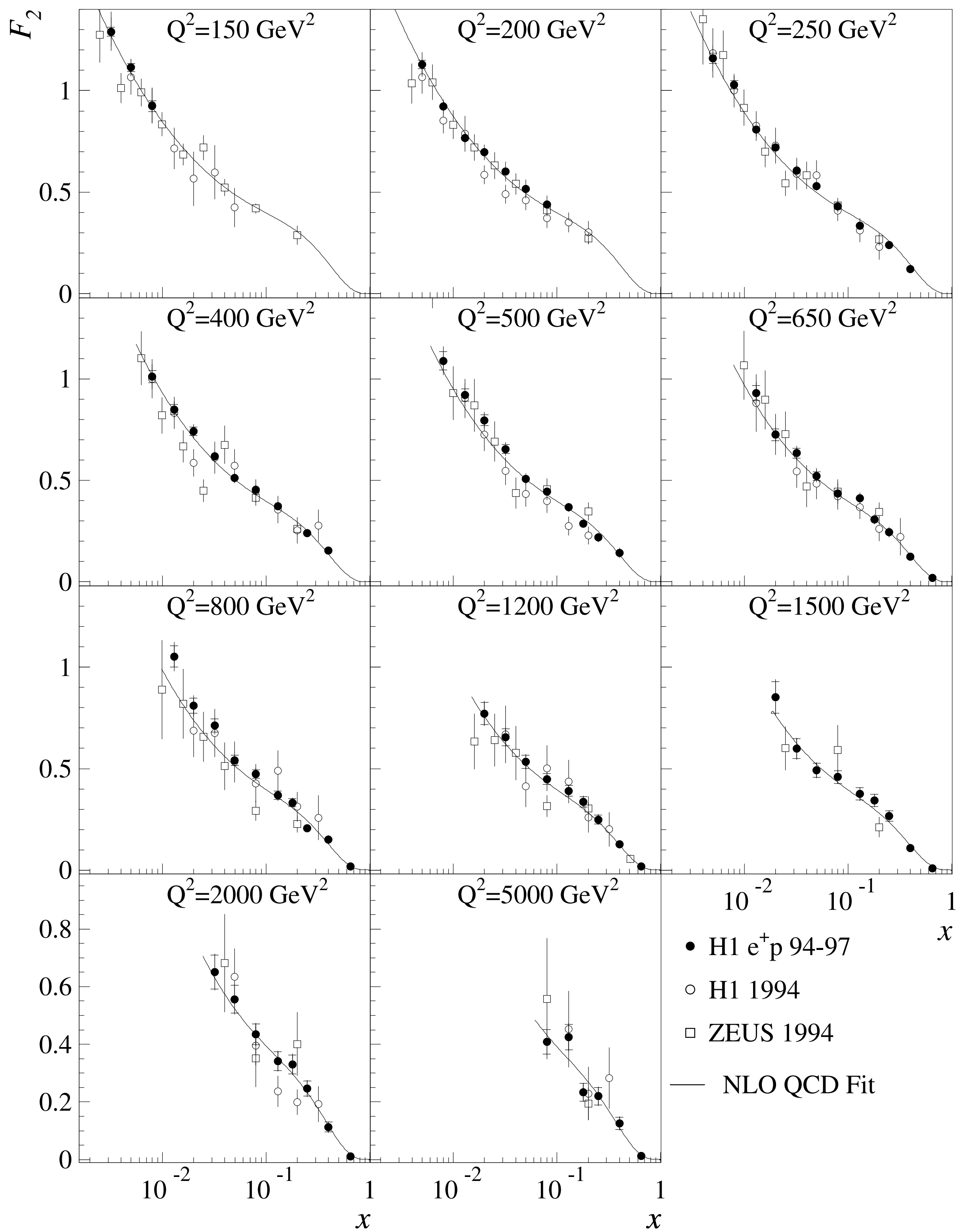

Figure 9: *Measurement of the electromagnetic structure function $F_2(x, Q^2)$ with the data taken between 94 and 97 (solid points). Also shown are the results obtained by H1 and ZEUS with the 94 data (open symbols). The inner error bars of the present data represent the statistical errors, the outer ones correspond to the total error.*

measurement by more than a factor of two with respect to the 1994 results is achieved. The new measured points are in agreement with the 1994 data, considering the large errors of the 1994 H1 and ZEUS measurements. Due to its superior precision, the new measurement supersedes the H1 1994 data at $Q^2 \geq 200~\mathrm{GeV}^2$ and at $Q^2 = 150~\mathrm{GeV}^2$ for $x < 10^{-2}$.

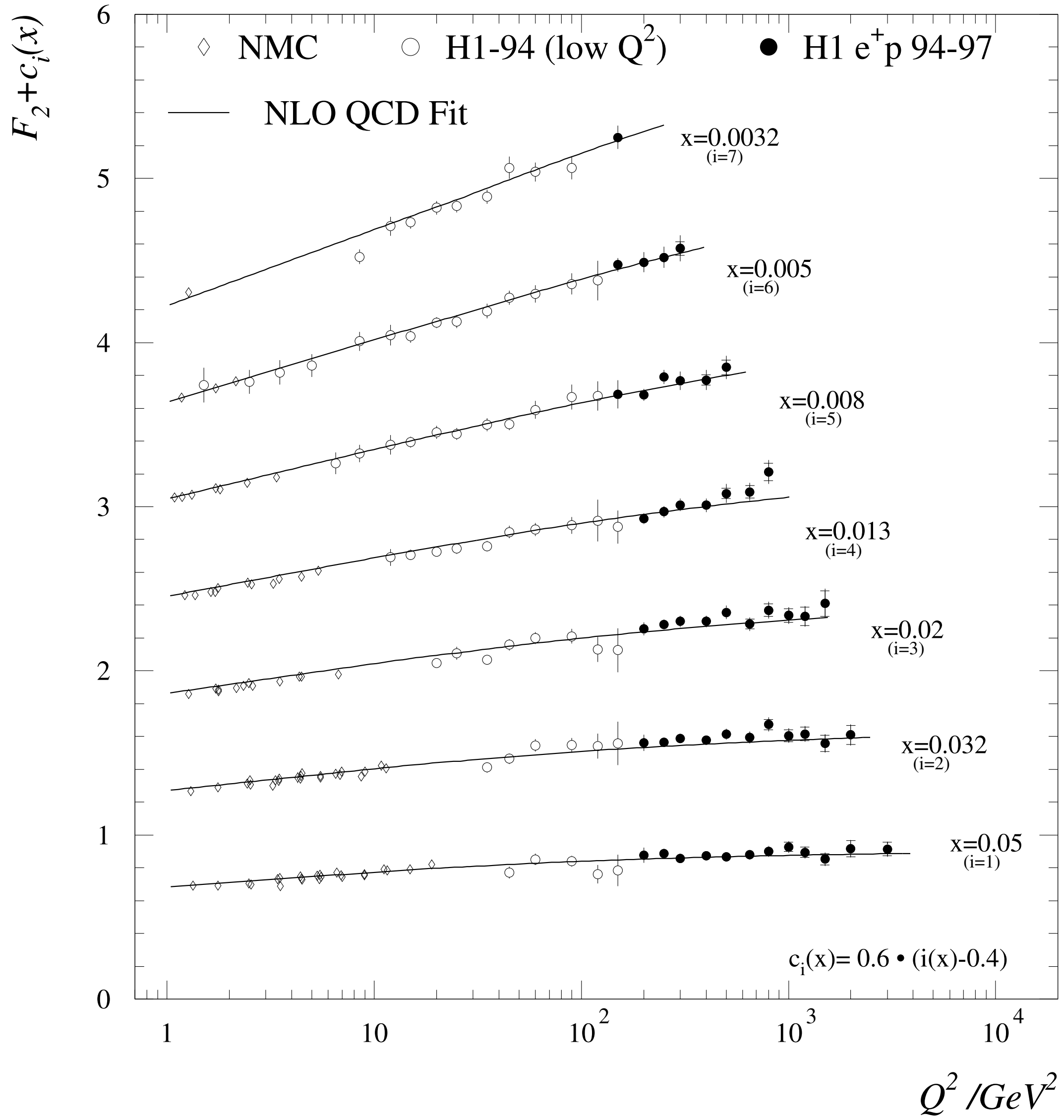

Figure 10: *Measurement of the electromagnetic structure function $F_2(x, Q^2)$ with the data taken between 94 and 97 (solid points) as a function of Q^2 for x values between 0.0032 and 0.05. Also shown are the results obtained by H1 at $Q^2 < 150~\mathrm{GeV}^2$ with the 94 data (open circles) and the NMC data (open squares). The outer (inner) error bars represent the total (statistical) errors.*

The F_2 measurements at low x ($x \leq 0.05$) are shown in fig. 10. as a function of Q^2. The high Q^2 data are compared with the published H1 1994 data [6] at $Q^2 < 150~\mathrm{GeV}^2$, and with the NMC [5] proton data, and found to be consistent. All the measured data points are described by the Q^2 evolution of F_2 predicted by the NLO DGLAP equations, from $Q^2 \approx 1~\mathrm{GeV}^2$ up to the highest measured Q^2. A positive slope as a function of Q^2 is visible for the low x data points and this slope decreases with increasing x as expected from QCD.

4.3 Measurement of the CC Cross-Section $d^2\sigma_{CC}/dxdQ^2$

The double differential cross-section $d^2\sigma_{CC}/dxdQ^2$, measured for $300 \leq Q^2 \leq 15\,000\ \mathrm{GeV}^2$ and for $0.013 \leq x \leq 0.4$, is listed in table 5. It is displayed in fig. 11 in the form of the reduced cross section (eq. 19). The uncertainties on the measurements are dominated by the statistical errors. The largest systematic errors come from the uncertainty on the energy scale of the hadronic final state and from the uncertainty on the trigger efficiency. The Standard Model cross-section, calculated using the NLO QCD Fit parton distributions, is found to agree well with the data.

At high x the e^+p CC cross-section is expected to be dominated by d quark scattering as is shown in fig. 11, which includes the expected d quark contribution to the CC cross-section, obtained from the NLO QCD Fit. The observed rise of $\tilde{\sigma}_{CC}$ as x decreases is explained in QCD by the contribution of $\bar{u}$ and $\bar{c}$ quarks from the sea. The contribution of d and s quarks is small at low x (equivalent to high y), due to the suppression by the $(1-y)^2$ term in eq. 21.

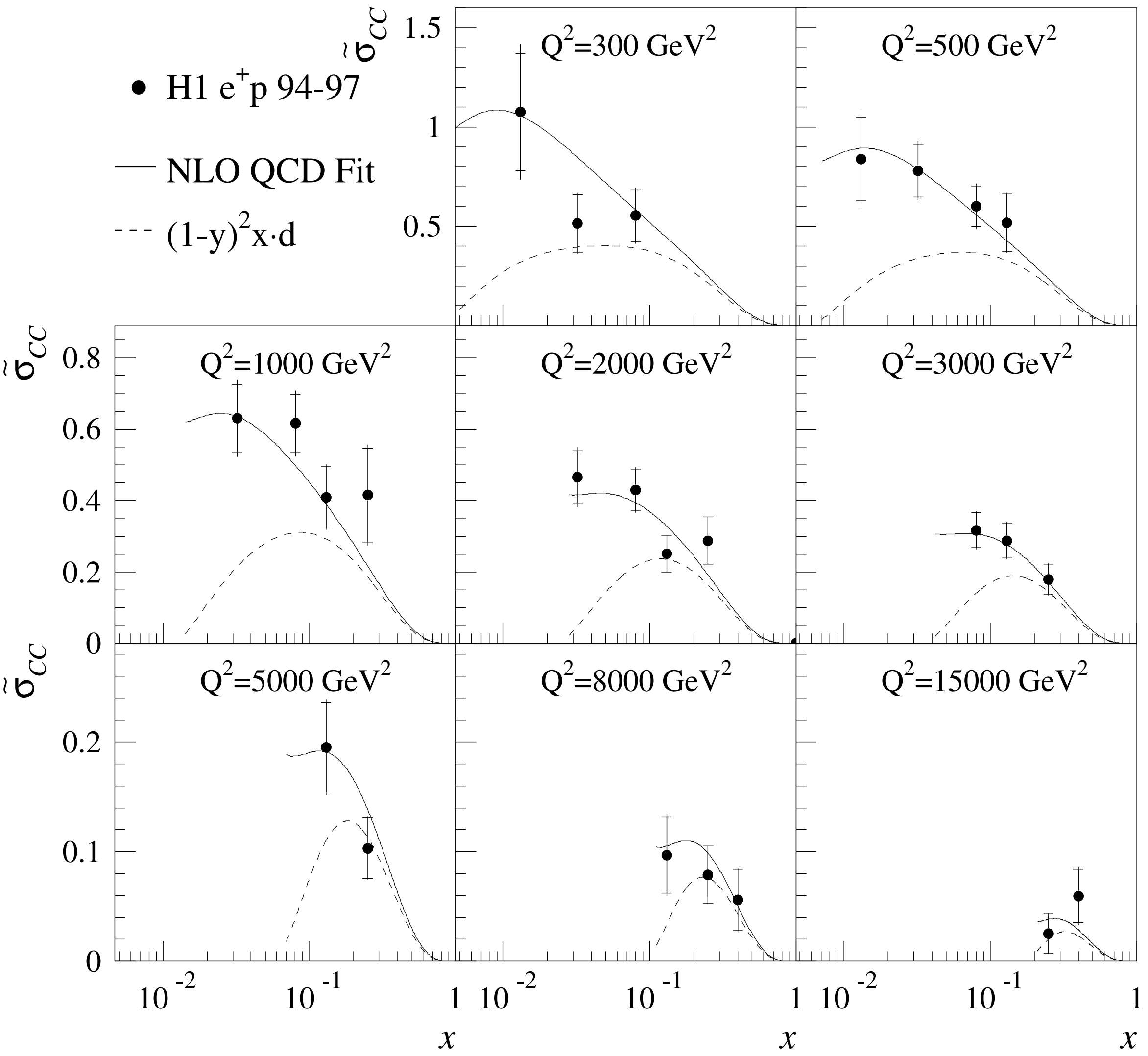

Figure 11: *CC reduced cross-section obtained from the double differential cross-section (as defined in eq. 19) is shown as a function of x for different Q^2 values and compared with the NLO QCD Fit. Also shown is the d quark contribution to the NLO QCD Fit. The inner error bars represent the statistical errors, the outer ones correspond to the total error.*

4.4 Helicity Structure of the NC and CC Cross-Sections

The double differential NC and CC cross-section measurements test the predictions of electroweak theory for the scattering of two fermions, and allow the contributions of individual quark flavours to be analyzed.

In the region of approximate Bjorken scaling, $x \approx 0.1$, the helicity dependence of the positron-quark interactions can be directly separated from the quark density distributions. In fig. 12 the measured structure function terms ϕ_{CC} and ϕ_{NC} are shown as a function of $(1-y)^2$. The latter observable is directly related to the scattering angle θ^* in the positron-quark centre of mass system through $\cos^2 \frac{\theta^*}{2} = 1 - y$.

The measurements of ϕ_{CC} are shown in figs. 12a-c. They are compatible with linear distributions in $(1-y)^2$. In leading order (eq. 21), these distributions are expected to result from two components reflecting the helicity structure of the CC interactions: an isotropic distribution from positron-antiquark scattering ($\bar{u}, \bar{c}$), and a distribution linearly rising with $(1-y)^2$ from positron-quark (d, s) scattering.

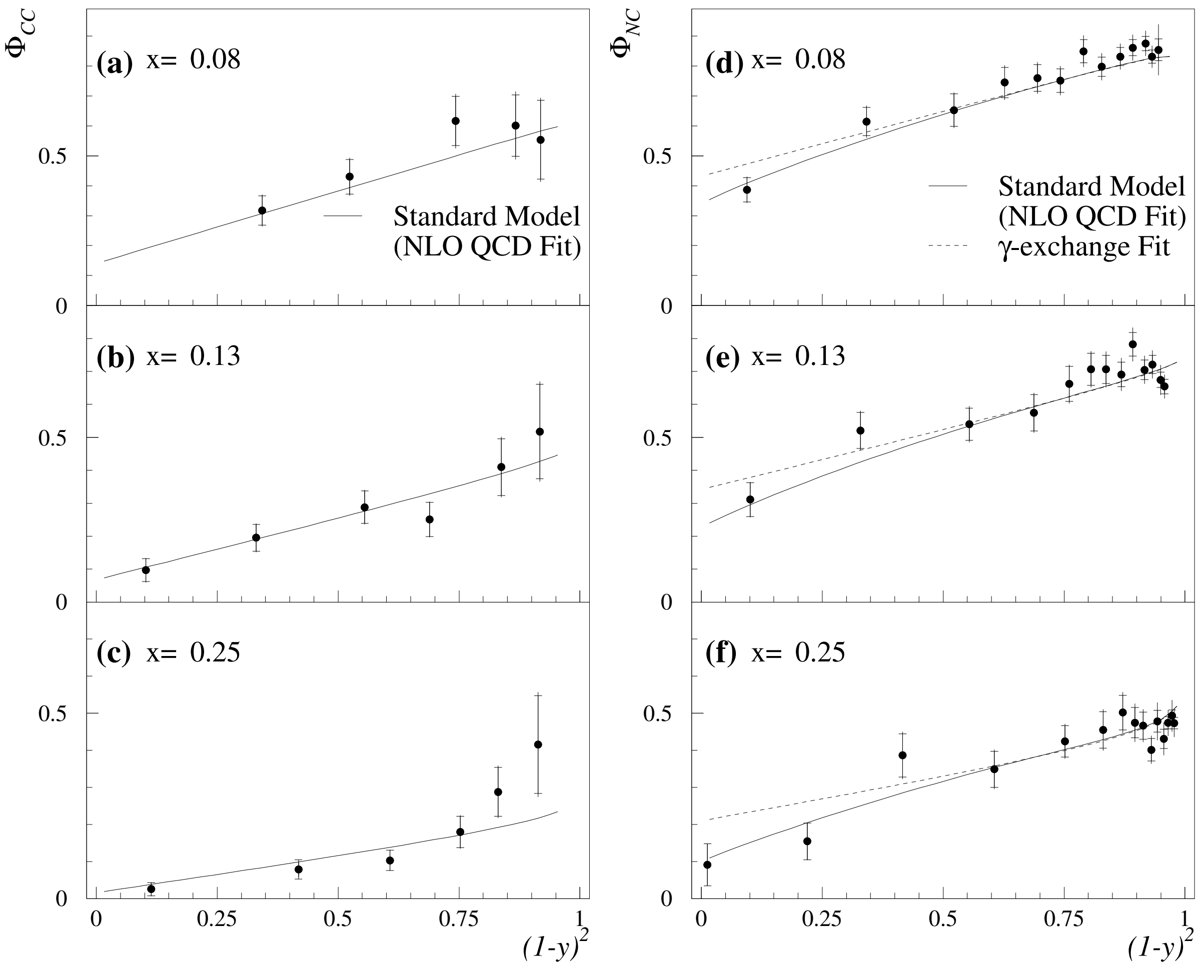

Figure 12: *Structure function terms ϕ_{CC} of the CC (a,b,c) and ϕ_{NC} of the NC (d,e,f) double differential cross-sections as a function of $(1-y)^2$ at $x = (0.08, 0.13, 0.25)$. The inner (outer) error bars represent the statistical (total) errors. The NLO QCD Fit (solid line) and the γ-exchange Fit (dashed line) are shown for comparison.*

The curves in figs. 12a-c represent the result of the NLO QCD Fit and show the two helicity components being of different magnitude. At $x = 0.08$ the contribution of the antiquarks which dominates as $(1-y)^2 \to 0$, is sizeable but decreases as x increases. The component rising with $(1-y)^2$ reflects the quark contribution which is larger than that of the antiquarks, as expected from the d valence quark density.

The measurements of ϕ_{NC} are shown in figs. 12d-f. In leading order (eq. 13), two helicity components are expected to contribute, however, with equal magnitude, since the NC processes are insensitive to the difference between quarks and antiquarks and their helicities.

The interference between the photon and Z° contributions in the NC measurement discussed in section 4.1 is also visible in figs. 12d-f: in the region of large $(1-y)^2$ the data follow the γ-exchange Fit reflecting essentially the two helicity components expected from photon exchange between the positron and the (anti)quarks. However, at small values of $(1-y)^2 = \left(1 - Q^2/(s\,x)\right)^2$, the data lie significantly below this fit hypothesis, in agreement with the Standard Model expectation.

4.5 Quark Densities from NC and CC Results at High x

The behaviour of the d/u ratio at high x is still a matter of debate [66]. The high Q^2 NC and CC cross-sections are sensitive to the PDFs at all x values, however, at high x in the valence quark region, the u and d quark distributions can be extracted from the cross-sections with minimal assumptions. Such an extraction is presented here for x values of 0.25 and 0.4.

The density of the sea quarks is expected to be small at high x, as can be inferred for CC interactions from fig. 12c. At high x the structure function term ϕ_{NC}, is primarily sensitive to the u quark density since the contribution from the d quark is suppressed due to the quark charge squared (eq.13). Conversely, ϕ_{CC} is sensitive mainly to the d density, since u quark scattering does not contribute in e^+p CC interactions.

Fig. 13a(c) and b(d) shows the NC (CC) structure function term at $x = 0.25$ and $x = 0.40$, the expectation of the Low Q^2 Fit for the structure function terms and the dominant contribution (ϕ^u_{NC} and ϕ^d_{CC}) of the corresponding valence quark: u for ϕ_{NC}, d for ϕ_{CC}, as obtained from the fit.

The data can also be displayed as xu and xd quark densities: the extraction of these densities in the $\overline{MS}$ scheme is done by multiplying the measured structure function term ϕ_{NC} and ϕ_{CC} by the following ratios, as obtained from the Low Q^2 Fit:

$$xu = \phi_{NC} \left[\frac{xu}{\phi_{NC}}\right]_{\text{Low Q}^2\text{ Fit}} \qquad\qquad xd = \phi_{CC} \left[\frac{xd}{\phi_{CC}}\right]_{\text{Low Q}^2\text{ Fit}} . \tag{27}$$

The results are shown in fig. 13e,f as a function of Q^2 and compared to the NLO QCD expectation of these densities. For this extraction, the error coming from the other quark densities is generally below 2% for the NC case and 7% for the CC case. This was estimated conservatively by varying the other parton densities by $\pm 50\%$. These errors are added in quadrature to the total errors of the data.

Although the errors are sizeable with the current data statistics, the ep measurements provide another determination of the d density in the proton, compared to the F_2^d fixed target measurements which require nuclear binding corrections for the parton density extraction.

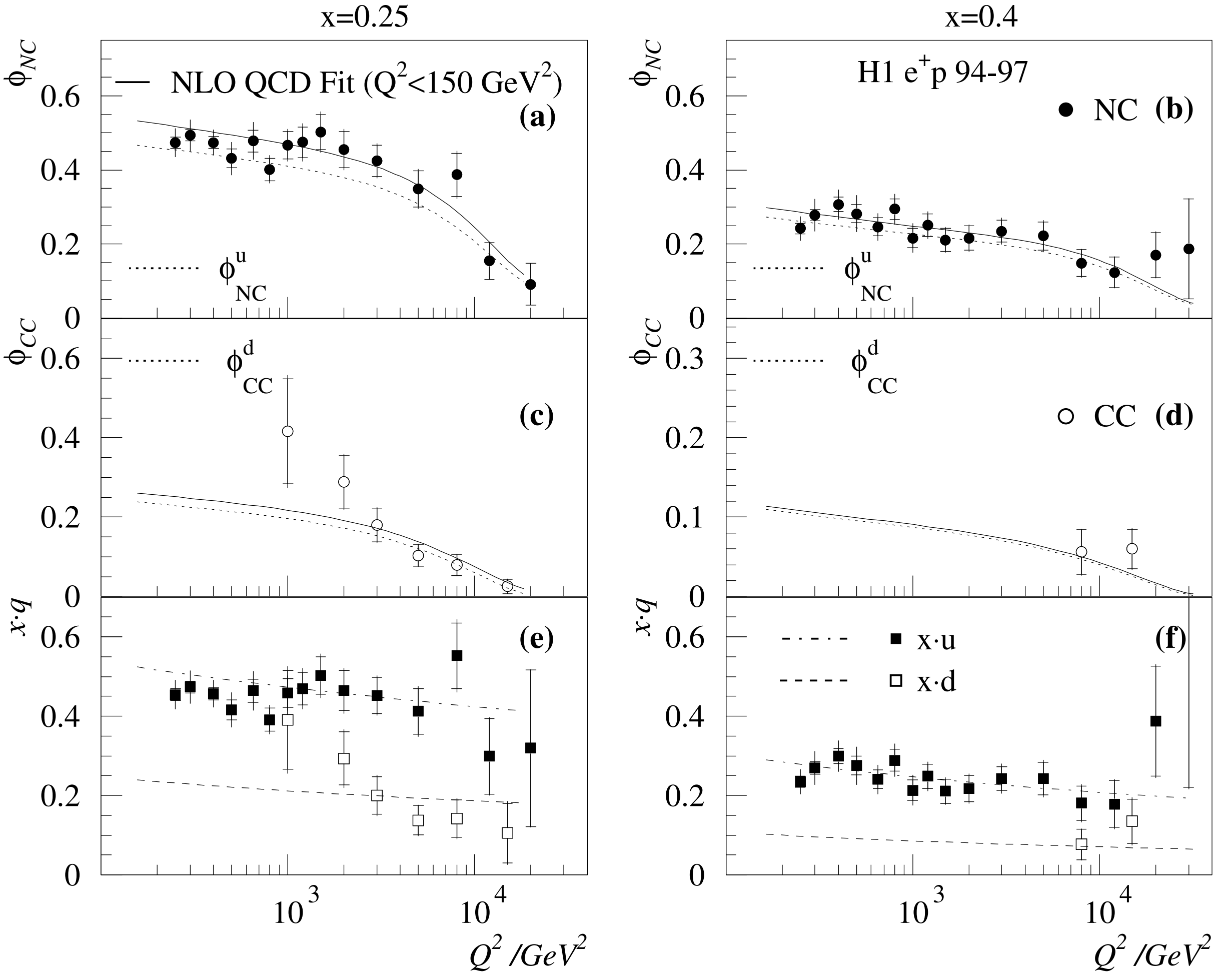

Figure 13: *Structure function terms of the NC and CC double differential cross-sections (ϕ_{NC} and ϕ_{CC}) as a function of Q^2 at $x = 0.25$ (a,c) and $x = 0.40$ (b,d). The inner error bars represent the statistical errors, the outer ones correspond to the total error. The extracted u and d quark densities are shown at $x = 0.25$ in (e) and $x = 0.4$ in (f), and compared to their QCD expectation as obtained from the Low Q^2 Fit.*

4.6 Measurement of the x Dependence of the NC and CC Cross-Sections

The NC(CC) single differential cross-sections $d\sigma_{NC(CC)}/dx$ are shown for $Q^2 > 1000\ \mathrm{GeV}^2$ in fig. 14a(b). The measurement extends in x from 0.013 to 0.65 (0.025 to 0.4). The cross-sections rise towards low x. The decrease of the cross-section at $x < 3 \cdot 10^{-2}$ is due to the kinematic cut $y < 0.9$. In this Q^2 range, the NC and CC cross-sections are still dominated by the scattering on low x sea partons.

The ratio of the measured $d\sigma_{NC(CC)}/dx$ cross-sections to the Standard Model expectation is shown in fig. 14c(d). Also shown is the uncertainty on the Standard Model, which was determined using the procedure described in section 3.2. All data agree well with the Standard Model expectation. The significance of the difference between the measurement of $d\sigma_{NC}/dx$ and the expectation at $x = 0.65$, is small when taking into account the systematic error and the uncertainty on the expectation.

The γ-exchange Fit also displayed in fig. 14a shows almost no difference with the Standard

Model expectation. This shows that NC scattering is still dominated by photon exchange at $Q^2 \approx 1000\ \mathrm{GeV}^2$.

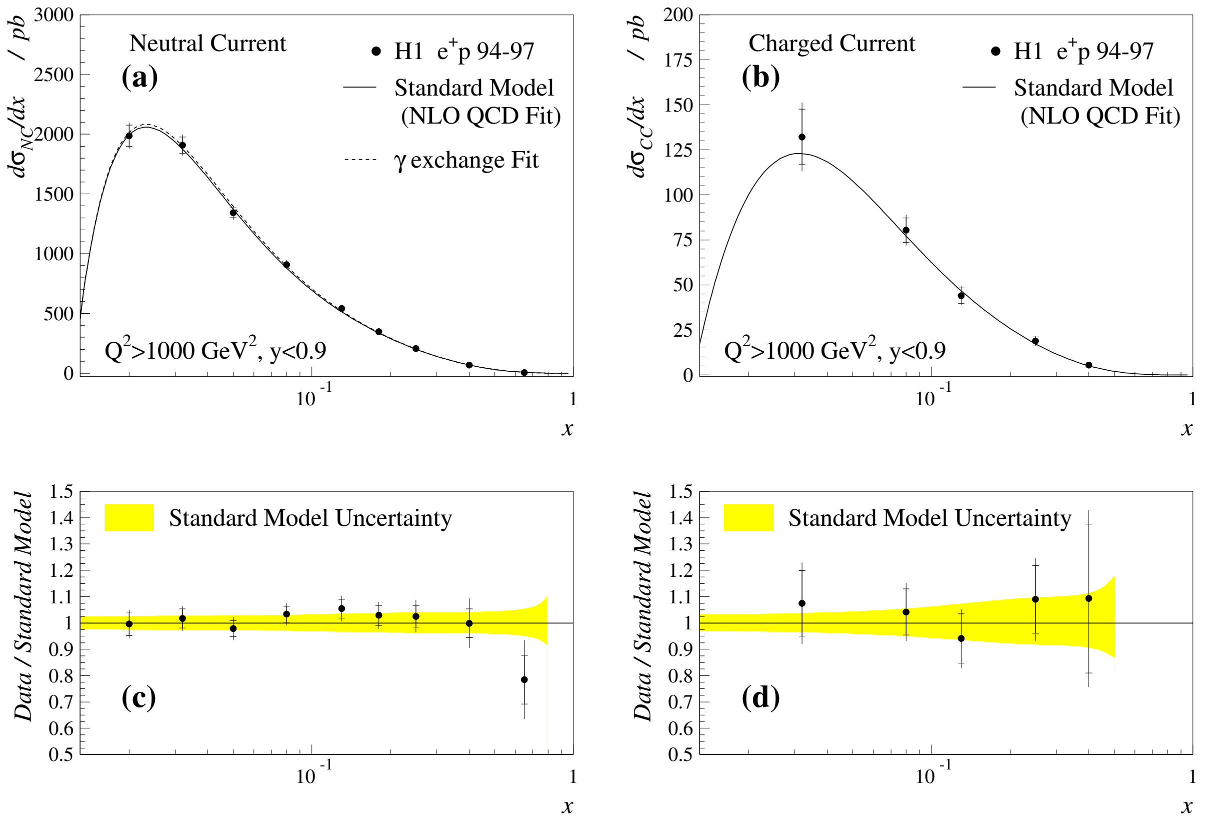

Figure 14: *(a) NC cross-section $d\sigma_{NC}/dx$ compared with the γ-exchange Fit (dashed line) and with the Standard Model expectation as obtained from the NLO QCD Fit (solid line). (b) CC cross-section $d\sigma_{CC}/dx$ compared with the Standard Model expectation (solid line). (c,d) NC,CC cross-sections divided by the Standard Model expectations. The shaded band in (c,d) represents the Standard Model uncertainty. The inner(outer) error bars represent the statistical(total) errors. The cross-sections are given for $Q^2 > 1000\ \mathrm{GeV}^2$ and $y < 0.9$.*

The results of the two fits are compared with $d\sigma_{NC}/dx$ for $Q^2 \geq 10\,000\ \ \mathrm{GeV}^2$(fig. 15). In contrast with what is observed for $Q^2 > 1000\ \mathrm{GeV}^2$, the two expectations are significantly different. The data agree with the Standard Model expectation and disagree with the γ-exchange Fit.

4.7 Measurement of the Q^2 Dependence of the NC and CC Cross-Sections

The NC(CC) single differential cross-sections $d\sigma_{NC(CC)}/dQ^2$ are shown in fig. 16a(b) and listed in table 6(7). Also shown is the Standard Model expectation given by the NLO QCD Fit described in section 3.2. The cross-sections have been corrected for a part of the cross-section that is unseen due to kinematic requirements (table 6 and 7). With this correction the NC and CC measurements are presented within the same kinematic range of $y < 0.9$. The statistical uncertainty is the dominating error at Q^2 above $1000\ \mathrm{GeV}^2$ for the NC cross-section, and at all Q^2 for the CC one. The systematic errors on these cross-sections are about 3% (8%) in the NC (CC) case.

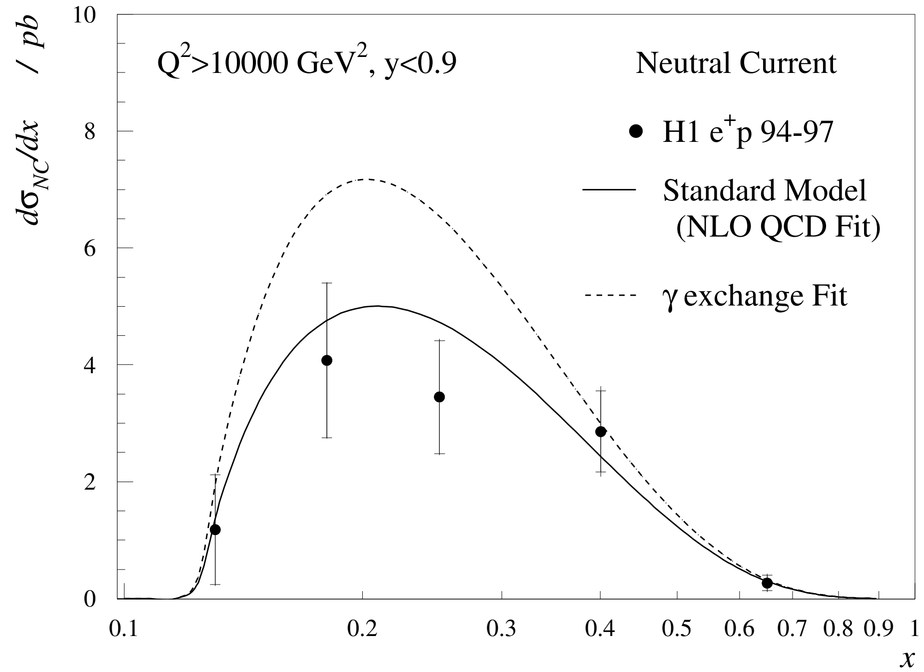

Figure 15: *NC cross-section $d\sigma_{NC}/dx$ at $Q^2 > 10\,000$ GeV^2 compared with the Standard Model expectation and with the expectation when the coupling to the Z° boson is not taken into account. The inner(outer) error bars represent the statistical(total) errors.*

The measurement of the NC cross-section spans more than two orders of magnitude in Q^2. The rapid fall of the cross-section with Q^2 by about 6 orders of magnitude is well reproduced by the Standard Model expectation. Figure 16c shows the ratio of the measured NC cross-section over the Standard Model expectation. The data at $Q^2 \leq 5000$ GeV^2, shown also in an enlarged figure inserted in fig. 16c, are well described by the NLO QCD Fit. The enhancement of the cross-section visible in the two highest Q^2 measurements is directly related to the excess discussed for $x = 0.4$ and $Q^2 > 15\,000$ GeV^2 in section 4.1. The Standard Model uncertainty shown in fig. 16c is based on the total errors of the fit discussed in section 3.2.

Due to the propagator mass term and to the different coupling, the CC cross-section shown in fig. 16b is smaller than the NC one and falls less steeply, by about 3 orders of magnitude between $Q^2 = 300$ and $15\,000$ GeV^2. Both shape and magnitude are well described by the Standard Model expectation.

4.8 Measurement of the W Boson Mass from the CC Cross-Section

Since CC interactions take place in the Standard Model by the t-channel exchange of a virtual W boson, the measurement of M_W in the space-like region permits an important test of electroweak theory [67]. The W boson mass arises in the propagator term, $(M_W^2/(Q^2 + M_W^2))^2$, of the CC cross-section (eq. 18). The universality of the Standard Model can be tested by comparing this result with the measurements in time-like processes and with indirect determinations of M_W, obtained by other experiments.

A fit of the CC cross-section that is sensitive only to the value of M_W from the propagator term, is performed by taking the Standard Model expectation of the CC cross-section as given in eq. 18 and allowing only M_W to vary. The Fermi constant G_F is set to its experimentally

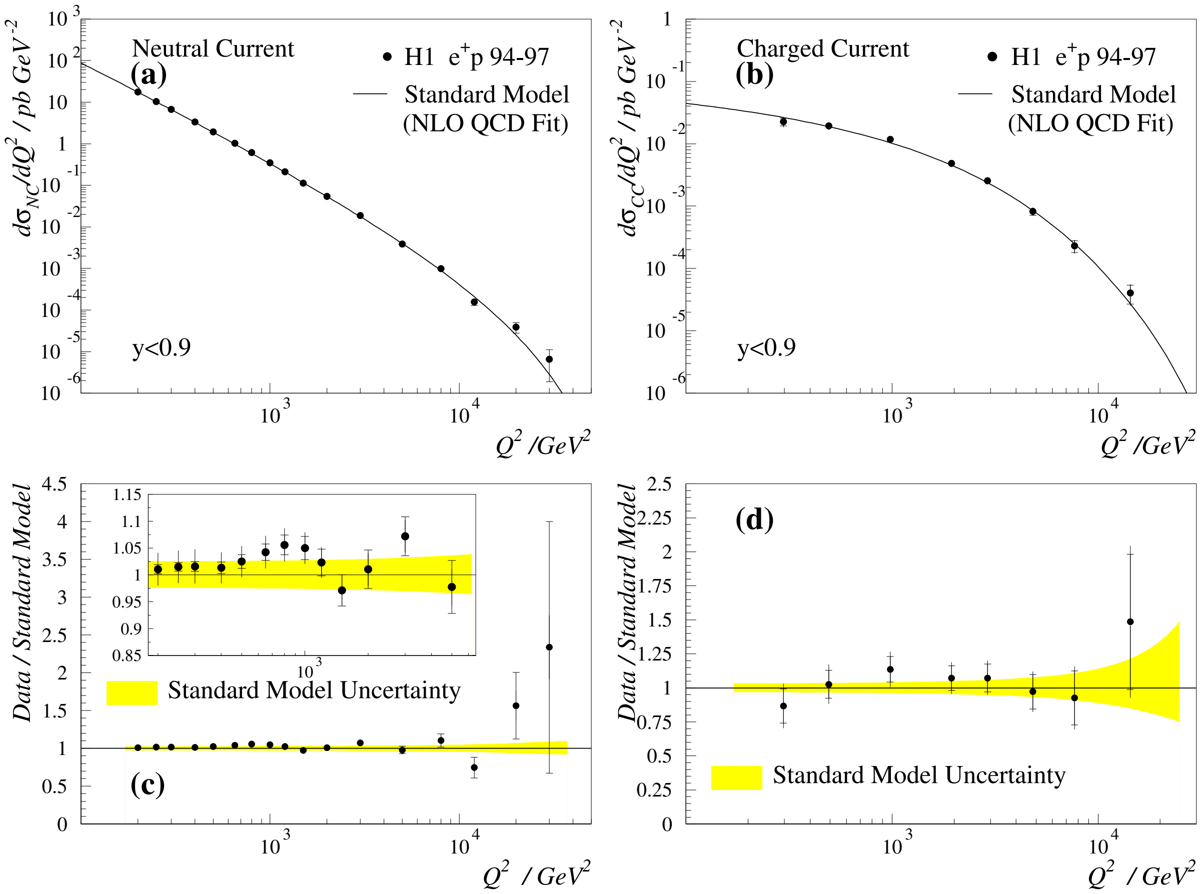

Figure 16: *NC and CC cross-sections $d\sigma_{NC}/dQ^2$ (a) and $d\sigma_{CC}/dQ^2$ (b) compared with the Standard Model expectation. Measured cross-section divided by the Standard Model expectation for NC (c) and CC (d). The shaded band in (c,d) represents the Standard Model uncertainty. The inner error bars represent the statistical errors, the outer ones correspond to the total error.*

determined value G_μ [54]. The expectation is calculated using the HECTOR program [51] with ϕ_{CC} evaluated using the PDFs from the Low Q^2 Fit[8]. The resulting Propagator Mass Fit, performed to the double differential CC cross-section data, has a χ^2/ndf of $19.9/(25-1) = 0.83$ and gives the value:

$$M_W = 80.9 \pm 3.3(\mathrm{stat.}) \pm 1.7(\mathrm{syst.}) \pm 3.7(\mathrm{theo.})\mathrm{GeV} \tag{28}$$

The Standard Model uncertainty is evaluated by varying the assumptions on the input Low Q^2 Fit as described in section 3.2. The largest contribution to this uncertainty comes from the parameterization of the $\bar{d}/\bar{u}$ asymmetry which leads to a shift of the W mass of 1.4 GeV [9]. The value of M_W extracted in the space-like regime is found to be in agreement with time-like determinations [69]. This result is illustrated in fig. 17 which compares the ratios of either the measured CC $d\sigma/dQ^2$ cross-section, or the Standard Model expectation from the Low Q^2 Fit, to the result of the Propagator Mass Fit.

[8]The weak radiative corrections have been taken into account for the theoretical predictions and have a negligible effect on the results.

[9]As described in section 3.2, the effect of an uncertainty of $\pm 50\%$ of the deuteron binding corrections is included in the theoretical error. However, if the deuteron binding correction is not performed, the resulting W mass is shifted by -0.7 GeV. If the correction proposed in [68] is applied the W mass is shifted by -1.7 GeV.

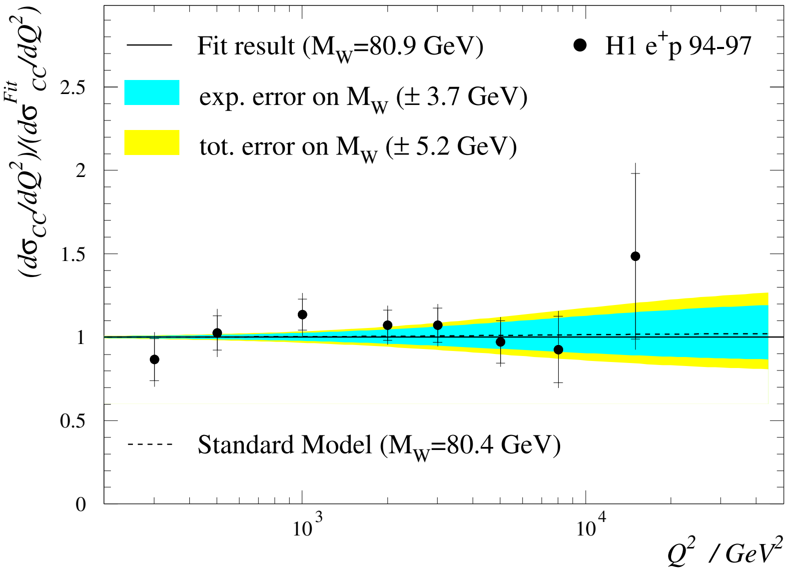

Figure 17: *CC cross-section $d\sigma_{CC}/dQ^2$ divided by the Propagator Mass Fit (see text). The dotted line shows similar ratio for the Standard Model expectation. The shaded bands indicate the uncertainties on the Propagator Mass Fit due to the experimental (± 3.7 GeV) and the total (± 5.2 GeV) error on M_W.*

5 Summary

Neutral and charged current processes with Q^2 between 150 and $30\,000$ GeV^2 and x between 0.0032 and 0.65 have been studied in e^+p collisions with the H1 detector at HERA using the data taken from 1994 to 1997. The increased integrated luminosity combined with the progress in the understanding of the detector response has permitted significantly more precise measurements at high Q^2. The double differential cross-section $d^2\sigma/dxdQ^2$ has been measured for NC and CC interactions in new kinematic domains.

The $d^2\sigma_{NC}/dxdQ^2$ cross-section have a typical precision of 5% for the bulk of the measurements. They are well described by a NLO QCD fit performed on the low Q^2 H1 and fixed target data (BCDMS and NMC). The inclusion of the high Q^2 data lowers the expectation from the fit of the low Q^2 data alone by about 3% at high x and high Q^2, and reduce the uncertainty of the expectation to 6% in this region. The test of perturbative QCD in DIS is extended with this measurement to higher Q^2, showing that the validity of the DGLAP equations extends over 4 orders of magnitude in Q^2.

The decrease of the cross-section expected in e^+p collisions at $Q^2 \gtrsim 8000$ GeV^2, due to the γZ° interference, is observed at high Q^2 for $0.08 \leq x \leq 0.25$. In contrast, at $x = 0.4$ and $Q^2 > 15\,000$ GeV^2 an enhancement of the cross-section compared to the expectation is visible. This effect has been reported in a previous publication based on the $1994-1996$ data alone. It has become less significant when adding the 1997 data. At the highest measured x ($x = 0.65$), the data are slightly below the expectation which is mainly constrained by the BCDMS data.

The $d^2\sigma_{CC}/dxdQ^2$ cross-section has been measured for Q^2 between 300 and $15\,000$ GeV^2 and for x between 0.013 and 0.4. The uncertainties on the measurements are dominated by the statistical errors. The Standard Model expectation agree well with the data.

The measured helicity dependencies of the NC and CC cross-sections are found to be consistent with Standard Model expectations. An extraction of the u and d quark densities at high

x ($x = 0.25, 0.4$), gives new and complementary information compared to the previous extractions of the valence quark densities from the scattering off hydrogen and deuterium targets.

The NC(CC) single differential cross-section $d\sigma_{NC(CC)}/dx$ has been presented for $Q^2 > 1000\ \mathrm{GeV}^2$ and $y < 0.9$. Both measurements are in agreement with the Standard Model expectation. At $Q^2 > 10\,000\ \mathrm{GeV}^2$ the NC $d\sigma_{NC}/dx$ cross-section has been shown to be in agreement with the Standard Model expectation and in disagreement with an expectation where the effects of the Z° exchange are removed.

The NC(CC) single differential cross-section $d\sigma_{NC(CC)}/dQ^2$ has been shown to be described by the Standard Model expectations. A fit to the Q^2 dependence of the CC double differential cross-section gives a mass $M_W = 80.9 \pm 5.2\ \mathrm{GeV}$. This value agrees well with the mass of the W boson as measured in time-like processes, thereby confirming the electroweak sector of the Standard Model in space-like lepton nucleon scattering.

Acknowledgements

We are grateful to the HERA machine group whose outstanding efforts have made and continue to make this experiment possible. We thank the engineers and technicians for their work in constructing and now maintaining the H1 detector, our funding agencies for financial support, the DESY technical staff for continual assistance, and the DESY directorate for the hospitality which they extend to the non-DESY members of the collaboration. We thank H. Spiesberger for useful discussions on the radiative corrections aspects of this measurement.

References

[1] E.D. Bloom et al., Phys. Rev. Lett. **23** (1969) 930;
M. Breidenbach et al., Phys. Rev. Lett. **23** (1969) 935.

[2] Gargamelle Neutrino Collab., F.J. Hasert et al., Phys. Lett. **B46** (1973) 138.

[3] D.J. Fox et al., Phys. Rev. Lett. **33** (1974) 1504;
Y. Watanabe et al., Phys. Rev. Lett. **35** (1975) 898;
H.L. Anderson et al., Phys. Rev. Lett. **38** (1977) 1450;
B.A. Gordon et al., Phys. Rev. Lett. **41** (1978) 615;
EMC Collab., J.J. Aubert et. al.,Nucl. Phys. **B213** (1983) 31;
CDHS Collab., H. Abramowicz et. al., Z. Phys., **C25** (1984) 29;
BEBC Collab., K. Varvell et al., Z.Phys. **C36** (1987) 1;
CDHSW Collab., P. Berge et. al., Z. Phys., **C49** (1991) 187;
CCFR Collab., P.Z.Quintas et. al., Phys Rev. Lett. **71** (1993) 1307;
E665 Collab., M. R. Adams et. al., Z. Phys **C67** (1995) 403.

[4] BCDMS Collab., A. Benvenuti et al., Phys. Lett. **B223** (1989) 485.

[5] NMC Collab., M. Arneodo et al., Phys. Lett. **B364** (1995) 107.

[6] H1 Collab., S. Aid et al., Nucl. Phys. **B470** (1996) 3.

[7] ZEUS Collab., M. Derrick et al., Z. Phys. **C72** (1996) 399.

[8] H1 Collab., I. Abt et al., Nucl. Phys. **B407** (1993) 515;
H1 Collab., T. Ahmed et al., Nucl. Phys. **B439** (1995) 471.

[9] ZEUS Collab., M. Derrick et al., Phys. Lett. **B316** (1993) 412;
ZEUS Collab., M. Derrick et al., Z. Phys. **C65** (1995) 379.

[10] Yu.L. Dokshitzer, Sov. Phys. JETP **46** (1977) 641;
V.N. Gribov and L.N. Lipatov, Sov. J. Nucl. Phys. **15** (1972) 438 and 675;
G. Altarelli and G. Parisi, Nucl. Phys. **B126** (1977) 297;
G. Curci, W. Furmanski and R. Petronzio, Nucl. Phys. **B175** (1980) 27;
W. Furmanski and R. Petronzio, Phys. Lett. **B97** (1980) 437.

[11] H1 Collab., T. Ahmed et al., Phys. Lett. **B324** (1994) 241;
H1 Collab., S. Aid et al., Z. Phys. **C67** (1995) 565;
H1 Collab., S. Aid et al., Phys. Lett. **B379** (1996) 319.

[12] ZEUS Collab., M. Derrick et al., Phys. Rev. Lett. **75** (1995) 1006;
ZEUS Collab., M. Derrick et al., Z. Phys. **C72** (1996) 47.

[13] H1 Collab., C. Adloff et al., Z. Phys. **C74** (1997) 191.

[14] ZEUS Collab., J. Breitweg et al., Z. Phys. **C74** (1997) 207.

[15] H1 Collab., C. Adloff et al., DESY 99-081 (1999), *submitted to Eur. Phys. J.*

[16] ZEUS Collab., J. Breitweg et al., DESY 99-56 (1999), *submitted to Eur. Phys. J.*

[17] ZEUS Collab., J. Breitweg et al., DESY 99-59 (1999), *submitted to Eur. Phys. J.*

[18] A. Blondel and F. Jacquet, Proceedings of the Study of an ep Facility for Europe
ed. U. Amaldi, DESY 79/48 (1979) 391.

[19] U. Bassler and G. Bernardi, Nucl. Instr. Meth. **A361** (1995) 197;
U. Bassler and G. Bernardi, Nucl. Instr. Meth. **A426** (1999) 583.

[20] H1 Collab., I. Abt et al., Nucl. Instr. Meth. **A386** (1997) 310 and 348.

[21] H1 Calorimeter Group, B. Andrieu et al., Nucl. Instr. Meth. **A336** (1993) 460.

[22] H1 Spacal Group, R.D. Appuhn et al., Nucl. Instr. Meth. **A386** (1997) 397.

[23] H1 Collab., "Luminosity Measurement in the H1 Experiment at HERA",
ICHEP 96-Warsaw (1996), pa 17-026.

[24] B. Heinemann, Ph.D. Thesis, Hamburg, *in preparation*.

[25] R. Brun et al., GEANT3 User's Guide, CERN-DD/EE-84-1 (1987).

[26] G. A. Schuler and H. Spiesberger, Proceedings of the Workshop Physics at HERA, vol. 3,
eds. W. Buchmüller, G. Ingelman, DESY (1992) 1419.

[27] A. Kwiatkowski, H. Spiesberger and H.-J. Möhring, Comp. Phys. Comm. **69** (1992) 155.

[28] G. Ingelman, Proceedings of the Workshop Physics at HERA, vol. 3,
eds. W. Buchmüller, G. Ingelman, DESY (1992) 1366.

[29] L. Lönnblad, Comp. Phys. Comm. **71** (1992) 15.

[30] T. Sjöstrand, M. Bengtsson, Comput. Phys. Commun. **43** (1987) 367.

[31] F. Jegerlehner, DESY 97-121, Procedings of the Workshop ”QCD and QED in Higher Orders”, Rheinsberg, Germany, 1996, Nucl. Phys. B (Proc Suppl.);
H. Burkhardt et al., Z. Phys. **C43** (1989) 497.

[32] A.D. Martin, W.J. Stirling and R.G. Roberts, Phys. Lett. **B306** (1993) 145;
A.D. Martin, W.J. Stirling and R.G. Roberts, Phys. Lett. **B309** (1993) 492.

[33] T. Sjöstrand, Comput. Phys. Commun. **82** (1994) 74.

[34] M. Glück, E. Reya and A. Vogt, Phys. Rev. **D46** (1992) 1973.

[35] A. Courau and P. Kessler, Phys. Rev. **D46** (1992) 117.

[36] S. Baranov et al., Proceedings of the Workshop Physics at HERA, vol. 3, eds. W. Buchmüller, G. Ingelman, DESY (1992) 478;
J.A.M. Vermaseren, Nucl. Phys. **B229** (1983) 347.

[37] U. Bauer, J.A.M. Vermaseren and D. Zeppenfeld, Nucl. Phys. **B375** (1992) 3.

[38] P. Bruel, Ph. D. Thesis, Orsay (1998).

[39] E. Chabert, Ph.D. Thesis, Marseille, *in preparation*.

[40] I. Negri, Ph.D. Thesis, Marseille (1998).

[41] H1 Collab., C. Adloff et al., Eur. Phys. J. **C5** (1998) 575.

[42] H1 Calorimeter Group, B. Andrieu et al., Nucl. Instr. Meth. **A344** (1994) 492;
H1 Calorimeter Group, B. Andrieu et al., Nucl. Instr. Meth. **A350** (1994) 57.

[43] H1 Calorimeter Group, B. Andrieu et al., Nucl. Instr. Meth. **A336** (1993) 499.

[44] S. Bentvelsen et al., Proceedings of the Workshop Physics at HERA, vol. 1, eds. W.Buchmüller, G.Ingelman, DESY (1992) 23;
C. Hoeger, ibid., 43.

[45] U. Bassler and G. Bernardi, Z. Phys. **C76** (1997) 223.

[46] H.P. Wellisch et al., MPI-PhE/94-03 (1994).

[47] H1 Collab., C. Adloff et al., Z. Phys. **C74** (1997) 221.

[48] H1 Collab., “Performance of the H1 Liquid Argon Calorimeter”, *in preparation*.

[49] H. Spiesberger, Nucl. Phys. **B349** (1991) 109.

[50] D.Yu. Bardin et al., Z. Phys. **C42** (1989) 679.

[51] A. Arbuzov et al., Comp. Phys. Commun. **94** (1996) 128.

[52] H. Spiesberger et al., Proceedings of the Workshop Physics at HERA, vol. 2, eds. W. Buchmüller, G. Ingelman, DESY (1992) 798.

[53] M. Klein and T. Riemann, Z. Phys. **C24** (1984) 151.

[54] PDG 98, C. Caso et al., Eur. Phys. J. **C3** (1998) 1.

[55] J. Blümlein et al., Proceedings of the Workshop Physics at HERA, vol. 1, eds. W. Buchmüller, G. Ingelman, DESY (1992) 67.

[56] H. Georgi and H. Politzer, Phys. Rev. **D14** (1976) 1829.

[57] L. Frankfurt and M. Strikman, Phys. Rep. **160** (1988) 235.

[58] J. Gomez et al., Phys. Rev. **D49** (1994) 4348.

[59] M. Botje, QCDNUM15 program, *write-up in preparation*;
J. Blümlein et al., Proceedings of the Workshop Future Physics at HERA ,
eds. G. Ingelman, A. De Roeck, R. Klanner, DESY (1996) 23.

[60] C. Pascaud and F. Zomer, LAL/95-05 (1995).

[61] A.D. Martin et al., Eur. Phys. J **C4** (1998) 463.

[62] CCFR Collab., A.O. Bazarko et al., Z. Phys. **C65** (1995) 189.

[63] H1 Collab., C. Adloff et al., Z. Phys. **C72** (1996) 593.

[64] A.D. Martin, W.J. Stirling and R.G. Roberts, Phys. Lett. **B387** (1996) 419.

[65] F. James, CERN Program Library, D506.

[66] U.K. Yang and A. Bodek, Phys. Rev. Lett. **82** (1999) 2467 and references therein.

[67] W. Hollik et al., Proceedings of the Workshop Physics at HERA, vol. 2, eds. W. Buchmüller, G. Ingelman, DESY (1992) 923.

[68] A. W. Thomas, W. Melnitchouk, hep-ph/9708484.

[69] CDF Collab., F. Abe et al., Phys. Rev. Lett. **75** (1995) 11;
DØ Collab., B. Abbott et al., Phys. Rev. Lett. **80** (1998) 3008;
ALEPH Collab., R. Barate et al., Phys. Lett. **B422** (1998) 384;
DELPHI Collab., P. Abreu et al., Eur. Phys. J. **C2** (1998) 581;
L3 Collab., M. Acciarri et al., Phys. Lett. **B413** (1997) 176;
OPAL Collab., K. Ackerstaff et al., Eur.Phys.J. **C1** (1998) 395.

Q^2 (GeV^2)	x	y	$\tilde{\sigma}_{NC}$	δ_{sta} (%)	δ_{sys} (%)	δ_{tot} (%)	F_2	Δ_{all} (%)	Δ_{F_2} (%)	Δ_{F_3} (%)	Δ_{F_L} (%)
150	.0032	0.518	1.240	1.8	5.2	5.5	1.291	−4.0	0.1	−0.1	−4.0
150	0.005	0.331	1.100	1.8	3.3	3.8	1.115	−1.3	0.1	−0.1	−1.3
150	0.008	0.207	0.920	2.9	8.9	9.3	0.924	−0.4	0.1	−0.1	−0.4
200	0.005	0.442	1.102	1.8	5.0	5.3	1.130	−2.5	0.2	−0.1	−2.5
200	0.008	0.276	0.915	1.9	3.5	4.0	0.922	−0.8	0.2	−0.1	−0.8
200	0.013	0.170	0.765	2.2	3.7	4.3	0.767	−0.2	0.2	−0.1	−0.2
200	0.020	0.110	0.696	2.6	4.9	5.5	0.696	−0.1	0.2	−0.1	−0.1
200	0.032	0.069	0.601	3.2	7.5	8.1	0.601	0.0	0.2	−0.1	0.0
200	0.050	0.044	0.516	3.7	8.2	9.0	0.516	0.0	0.2	−0.1	0.0
200	0.080	0.028	0.439	4.2	9.0	9.9	0.439	0.0	0.1	−0.1	0.0
250	0.005	0.552	1.113	2.3	5.1	5.6	1.161	−4.1	0.2	−0.2	−4.1
250	0.008	0.345	1.018	2.0	3.7	4.2	1.031	−1.2	0.2	−0.1	−1.2
250	0.013	0.212	0.807	2.1	3.9	4.4	0.810	−0.4	0.2	−0.1	−0.4
250	0.020	0.138	0.721	2.1	3.6	4.1	0.721	−0.1	0.2	−0.1	−0.1
250	0.032	0.086	0.606	2.2	3.6	4.3	0.606	0.0	0.2	−0.1	0.0
250	0.050	0.055	0.529	2.4	3.4	4.2	0.529	0.0	0.2	−0.1	0.0
250	0.080	0.035	0.430	2.7	3.6	4.5	0.430	0.0	0.2	−0.1	0.0
250	0.130	0.021	0.334	3.4	4.3	5.5	0.334	0.0	0.2	−0.1	0.0
250	0.250	0.011	0.240	3.3	7.4	8.1	0.239	0.1	0.2	0.0	0.0
250	0.400	0.007	0.122	5.9	12.1	13.4	0.122	0.1	0.2	0.0	0.0
300	0.005	0.663	1.139	3.4	5.6	6.5	1.214	−6.2	0.3	−0.2	−6.2
300	0.008	0.414	0.989	2.4	5.1	5.7	1.008	−1.9	0.3	−0.2	−1.9
300	0.013	0.255	0.846	2.4	3.8	4.5	0.851	−0.6	0.3	−0.2	−0.6
300	0.020	0.166	0.740	2.4	3.9	4.6	0.742	−0.2	0.3	−0.2	−0.2
300	0.032	0.104	0.629	2.4	3.7	4.4	0.630	0.0	0.2	−0.1	−0.1
300	0.050	0.066	0.499	2.6	3.6	4.5	0.499	0.0	0.2	−0.1	0.0
300	0.080	0.041	0.456	2.7	3.9	4.8	0.456	0.0	0.2	−0.1	0.0
300	0.130	0.025	0.346	3.4	5.8	6.8	0.346	0.1	0.2	−0.1	0.0
300	0.250	0.013	0.250	3.1	8.1	8.7	0.250	0.1	0.2	−0.1	0.0
300	0.400	0.008	0.140	5.7	14.5	15.6	0.140	0.1	0.2	0.0	0.0
400	0.008	0.552	0.976	3.1	5.1	6.0	1.013	−3.6	0.4	−0.3	−3.5
400	0.013	0.340	0.841	2.8	3.9	4.8	0.850	−1.1	0.4	−0.3	−1.0
400	0.020	0.221	0.739	2.8	3.7	4.7	0.742	−0.4	0.4	−0.3	−0.3
400	0.032	0.138	0.619	2.8	3.6	4.6	0.619	−0.1	0.4	−0.2	−0.1
400	0.050	0.088	0.513	3.0	3.8	4.8	0.513	0.0	0.4	−0.2	0.0
400	0.080	0.055	0.455	3.1	4.0	5.1	0.455	0.0	0.3	−0.2	0.0
400	0.130	0.034	0.373	3.8	4.5	5.9	0.373	0.1	0.3	−0.1	0.0
400	0.250	0.018	0.241	3.5	6.5	7.4	0.241	0.1	0.3	−0.1	0.0
400	0.400	0.011	0.155	6.2	11.6	13.2	0.155	0.1	0.3	−0.1	0.0

Table 4: *NC reduced cross-section $\tilde{\sigma}_{NC}(x,Q^2)$ as obtained by dividing $d^2\sigma_{NC}/dxdQ^2$ by the kinematic factor $xQ^4/(Y_+2\pi\alpha^2)$, with statistical error (δ_{sta}), systematic error (δ_{sys}) and total error (δ_{tot}). The electromagnetic proton structure function $F_2(x,Q^2)$ is then given, together with Δ_{F_2}, Δ_{F_3}, Δ_{F_L} (which are the corrections due to $\tilde{F}_2$, $\tilde{F}_3$ and $\tilde{F}_L$ used to calculate F_2) and Δ_{all} as defined in eq. 17, i.e. $1+\Delta_{all} = (1+\Delta_{F_2}+\Delta_{F_3}+\Delta_{F_L})/(1+\delta^{weak}_{NC})$. The normalization uncertainty, which is not included in the systematic error, is 1.5%. The table continues on the next 2 pages.*

Q^2 (GeV^2)	x	y	$\tilde{\sigma}_{NC}$	δ_{sta} (%)	δ_{sys} (%)	δ_{tot} (%)	F_2	Δ_{all} (%)	Δ_{F_2} (%)	Δ_{F_3} (%)	Δ_{F_L} (%)
500	0.008	0.690	1.026	4.2	5.1	6.6	1.091	−6.0	0.5	−0.5	−5.8
500	0.013	0.425	0.906	3.3	5.2	6.2	0.922	−1.8	0.5	−0.5	−1.6
500	0.020	0.276	0.792	3.3	3.9	5.2	0.797	−0.6	0.5	−0.4	−0.5
500	0.032	0.173	0.654	3.3	4.0	5.2	0.655	−0.2	0.5	−0.4	−0.2
500	0.050	0.110	0.508	3.5	4.1	5.4	0.509	0.0	0.5	−0.3	−0.1
500	0.080	0.069	0.445	3.6	3.7	5.2	0.445	0.0	0.5	−0.3	0.0
500	0.130	0.042	0.368	4.3	4.3	6.1	0.367	0.1	0.4	−0.2	0.0
500	0.180	0.031	0.287	4.9	5.4	7.3	0.286	0.1	0.4	−0.2	0.0
500	0.250	0.022	0.220	5.9	8.5	10.4	0.220	0.1	0.4	−0.1	0.0
500	0.400	0.014	0.143	8.6	15.3	17.5	0.143	0.2	0.4	−0.1	0.0
650	0.013	0.552	0.903	4.0	4.3	5.9	0.933	−3.2	0.7	−0.8	−3.0
650	0.020	0.359	0.718	4.1	3.9	5.7	0.727	−1.2	0.7	−0.8	−0.9
650	0.032	0.224	0.633	4.0	4.0	5.7	0.635	−0.4	0.7	−0.7	−0.3
650	0.050	0.144	0.521	4.1	3.9	5.7	0.522	−0.1	0.7	−0.6	−0.1
650	0.080	0.090	0.436	4.0	4.0	5.7	0.436	0.0	0.7	−0.5	0.0
650	0.130	0.055	0.413	4.6	4.7	6.6	0.413	0.1	0.6	−0.4	0.0
650	0.180	0.040	0.309	5.3	5.8	7.9	0.309	0.1	0.6	−0.3	0.0
650	0.250	0.029	0.246	6.2	8.7	10.6	0.246	0.2	0.6	−0.2	0.0
650	0.400	0.018	0.125	9.9	11.5	15.2	0.125	0.2	0.5	−0.2	0.0
650	0.650	0.011	0.021	14.3	15.7	21.3	0.020	0.3	0.5	−0.1	0.0
800	0.013	0.680	1.000	5.0	4.7	6.8	1.055	−5.2	1.0	−1.2	−4.7
800	0.020	0.442	0.796	4.6	4.3	6.3	0.812	−1.9	1.0	−1.1	−1.5
800	0.032	0.276	0.709	4.5	4.0	6.0	0.714	−0.7	1.0	−1.0	−0.4
800	0.050	0.177	0.540	4.6	3.9	6.0	0.542	−0.3	0.9	−0.9	−0.1
800	0.080	0.110	0.474	4.6	4.2	6.2	0.474	−0.1	0.9	−0.7	0.0
800	0.130	0.068	0.370	5.4	4.8	7.2	0.369	0.1	0.9	−0.6	0.0
800	0.180	0.049	0.333	6.0	4.9	7.8	0.333	0.2	0.8	−0.4	0.0
800	0.250	0.035	0.208	7.5	5.8	9.4	0.208	0.2	0.8	−0.3	0.0
800	0.400	0.022	0.150	9.6	10.5	14.2	0.150	0.3	0.7	−0.2	0.0
800	0.650	0.014	0.018	19.6	18.4	26.9	0.018	0.3	0.6	−0.2	0.0
1000	0.020	0.552	0.754	5.4	3.8	6.6	0.779	−3.2	1.4	−1.8	−2.5
1000	0.032	0.345	0.639	5.6	4.1	6.9	0.647	−1.2	1.3	−1.6	−0.7
1000	0.050	0.221	0.566	5.1	3.8	6.4	0.569	−0.5	1.3	−1.4	−0.2
1000	0.080	0.138	0.431	5.3	3.7	6.5	0.432	−0.2	1.2	−1.1	−0.1
1000	0.130	0.085	0.385	6.1	4.8	7.7	0.384	0.0	1.2	−0.9	0.0
1000	0.180	0.061	0.341	6.7	4.3	7.9	0.340	0.2	1.1	−0.7	0.0
1000	0.250	0.044	0.244	7.8	5.4	9.5	0.243	0.3	1.0	−0.5	0.0
1000	0.400	0.028	0.111	12.1	13.4	18.1	0.111	0.4	1.0	−0.3	0.0
1000	0.650	0.017	0.013	25.0	15.1	29.2	0.013	0.5	0.9	−0.2	0.0
1200	0.020	0.663	0.737	7.2	3.7	8.1	0.774	−4.8	1.8	−2.5	−3.7
1200	0.032	0.414	0.645	6.4	3.8	7.4	0.657	−1.9	1.7	−2.3	−1.0
1200	0.050	0.265	0.531	6.0	3.5	6.9	0.536	−0.9	1.7	−2.0	−0.3
1200	0.080	0.166	0.448	5.9	3.6	6.9	0.450	−0.4	1.6	−1.6	−0.1
1200	0.130	0.102	0.391	6.8	3.7	7.8	0.391	0.0	1.5	−1.2	0.0
1200	0.180	0.074	0.338	7.5	4.7	8.9	0.337	0.1	1.4	−1.0	0.0
1200	0.250	0.053	0.250	8.7	6.7	10.9	0.249	0.3	1.4	−0.8	0.0

Q^2 (GeV^2)	x	y	$\tilde{\sigma}_{NC}$	δ_{sta} (%)	δ_{sys} (%)	δ_{tot} (%)	F_2	Δ_{all} (%)	Δ_{F_2} (%)	Δ_{F_3} (%)	Δ_{F_L} (%)
1200	0.400	0.033	0.129	12.1	8.5	14.8	0.129	0.5	1.2	−0.5	0.0
1200	0.650	0.020	0.017	24.2	17.5	29.9	0.017	0.6	1.1	−0.3	0.0
1500	0.020	0.828	0.789	9.2	5.0	10.5	0.855	−7.7	2.4	−3.5	−6.1
1500	0.032	0.518	0.581	8.1	4.3	9.2	0.601	−3.2	2.4	−3.5	−1.7
1500	0.050	0.331	0.486	7.2	3.8	8.1	0.494	−1.6	2.3	−3.0	−0.4
1500	0.080	0.207	0.457	6.8	3.7	7.8	0.461	−0.8	2.2	−2.5	−0.1
1500	0.130	0.127	0.376	8.0	3.9	8.9	0.377	−0.2	2.1	−1.9	0.0
1500	0.180	0.092	0.345	8.6	4.2	9.6	0.345	0.1	2.0	−1.5	0.0
1500	0.250	0.066	0.268	9.4	5.8	11.0	0.267	0.4	1.9	−1.1	0.0
1500	0.400	0.041	0.110	14.6	7.8	16.6	0.109	0.7	1.7	−0.8	0.0
1500	0.650	0.025	0.009	37.8	19.6	42.6	0.009	0.8	1.6	−0.5	0.0
2000	0.032	0.690	0.614	9.0	4.1	9.9	0.653	−6.1	3.6	−5.9	−3.2
2000	0.050	0.442	0.541	8.7	4.3	9.7	0.559	−3.2	3.5	−5.3	−0.9
2000	0.080	0.276	0.428	8.3	3.9	9.1	0.436	−1.7	3.3	−4.3	−0.2
2000	0.130	0.170	0.340	9.6	4.3	10.6	0.343	−0.7	3.1	−3.3	−0.1
2000	0.180	0.123	0.331	10.1	4.8	11.1	0.331	−0.1	3.0	−2.6	0.0
2000	0.250	0.088	0.249	10.7	5.9	12.2	0.248	0.4	2.8	−2.0	0.0
2000	0.400	0.055	0.114	15.1	8.2	17.2	0.113	0.9	2.6	−1.3	0.0
2000	0.650	0.034	0.011	37.8	18.7	42.2	0.011	1.2	2.3	−0.8	0.0
3000	0.050	0.663	0.513	7.3	4.1	8.4	0.558	−8.0	6.0	−11.0	−2.2
3000	0.080	0.414	0.458	7.7	4.2	8.7	0.481	−4.8	5.8	−9.3	−0.5
3000	0.130	0.255	0.347	9.1	4.8	10.2	0.356	−2.3	5.4	−7.0	−0.1
3000	0.180	0.184	0.324	9.2	4.1	10.0	0.327	−1.0	5.1	−5.5	0.0
3000	0.250	0.133	0.242	9.9	4.9	11.1	0.242	0.1	4.8	−4.2	0.0
3000	0.400	0.083	0.127	12.5	9.0	15.4	0.126	1.3	4.4	−2.7	0.0
3000	0.650	0.051	0.012	30.1	14.9	33.6	0.012	2.0	4.0	−1.6	0.0
5000	0.080	0.690	0.353	10.4	4.7	11.4	0.412	−14.3	10.8	−22.3	−1.8
5000	0.130	0.425	0.392	10.4	5.0	11.6	0.429	−8.7	10.1	−17.5	−0.4
5000	0.180	0.307	0.223	13.4	4.5	14.1	0.235	−5.1	9.6	−13.7	−0.1
5000	0.250	0.221	0.217	13.9	6.6	15.4	0.222	−2.1	9.0	−10.3	−0.1
5000	0.400	0.138	0.127	17.1	8.8	19.3	0.126	1.1	8.3	−6.5	0.0
5000	0.650	0.085	0.012	37.8	14.9	40.6	0.012	3.0	7.5	−4.0	0.0
8000	0.130	0.680	0.283	16.5	4.9	17.2	0.367	−23.0	16.6	−37.1	−1.2
8000	0.180	0.491	0.284	15.5	6.4	16.7	0.338	−16.0	15.6	−30.1	−0.4
8000	0.250	0.353	0.273	15.1	7.0	16.6	0.300	−9.0	14.7	−22.6	−0.1
8000	0.400	0.221	0.093	24.2	9.9	26.2	0.094	−1.5	13.5	−14.2	0.0
8000	0.650	0.136	0.013	44.7	19.8	48.9	0.012	3.1	12.3	−8.5	0.0
12000	0.180	0.736	0.153	34.4	4.3	34.6	0.232	−34.3	22.2	−53.9	−1.1
12000	0.250	0.530	0.127	32.1	6.2	32.7	0.165	−23.5	20.9	−42.6	−0.4
12000	0.400	0.331	0.085	33.3	11.4	35.2	0.093	−8.8	19.2	−26.9	−0.1
12000	0.650	0.204	0.015	57.7	24.2	62.6	0.015	0.8	17.4	−15.9	0.0
20000	0.250	0.884	0.090	61.9	5.5	62.2	0.188	−52.0	29.2	−78.3	−1.3
20000	0.400	0.552	0.142	35.7	9.9	37.0	0.206	−31.1	26.9	−56.3	−0.3
20000	0.650	0.340	0.021	70.7	41.6	82.0	0.023	−10.0	24.4	−33.4	0.0
30000	0.400	0.828	0.182	71.9	9.6	72.6	0.438	−58.5	32.7	−88.7	−0.7

Q^2 (GeV^2)	x	y	$d^2\sigma/dxdQ^2$ (pb/GeV^2)	ϕ_{CC}	δ_{sta} (%)	δ_{sys} (%)	δ_{tot} (%)	δ_{CC}^{qed} (%)
300	0.013	0.255	$0.637 \cdot 10^{0}$	1.075	27.4	16.0	31.8	+1.2
300	0.032	0.104	$0.124 \cdot 10^{0}$	0.514	28.1	10.3	30.0	+1.9
300	0.080	0.041	$0.532 \cdot 10^{-1}$	0.553	23.8	7.5	25.5	+2.5
500	0.013	0.425	$0.468 \cdot 10^{0}$	0.838	25.1	15.7	29.7	+0.3
500	0.032	0.173	$0.177 \cdot 10^{0}$	0.781	17.0	8.7	19.2	+0.4
500	0.080	0.069	$0.546 \cdot 10^{-1}$	0.601	17.0	6.5	18.9	+1.5
500	0.130	0.043	$0.289 \cdot 10^{-1}$	0.518	27.8	8.0	29.4	+1.4
1000	0.032	0.345	$0.124 \cdot 10^{0}$	0.630	15.0	8.0	17.1	+0.2
1000	0.080	0.138	$0.487 \cdot 10^{-1}$	0.616	13.3	6.1	14.8	−0.1
1000	0.130	0.085	$0.199 \cdot 10^{-1}$	0.410	20.9	6.5	22.5	0.0
1000	0.250	0.044	$0.105 \cdot 10^{-1}$	0.415	31.7	11.7	34.1	−1.0
2000	0.032	0.690	$0.716 \cdot 10^{-1}$	0.466	15.7	8.8	18.1	−2.9
2000	0.080	0.276	$0.264 \cdot 10^{-1}$	0.430	13.5	5.8	14.8	−2.5
2000	0.130	0.170	$0.949 \cdot 10^{-2}$	0.251	20.6	5.7	21.4	+0.1
2000	0.250	0.088	$0.566 \cdot 10^{-2}$	0.288	23.0	7.3	24.6	−0.6
3000	0.080	0.414	$0.156 \cdot 10^{-1}$	0.317	15.2	6.7	16.8	−2.6
3000	0.130	0.255	$0.872 \cdot 10^{-2}$	0.288	17.0	5.9	18.1	−4.1
3000	0.250	0.133	$0.283 \cdot 10^{-2}$	0.180	23.6	8.2	25.1	−1.6
5000	0.130	0.425	$0.402 \cdot 10^{-2}$	0.195	21.0	7.4	22.3	−4.9
5000	0.250	0.221	$0.111 \cdot 10^{-2}$	0.103	26.8	6.5	27.6	−4.1
8000	0.130	0.680	$0.125 \cdot 10^{-2}$	0.097	35.7	14.3	38.5	−8.2
8000	0.250	0.354	$0.530 \cdot 10^{-3}$	0.079	33.5	11.2	35.4	−5.3
8000	0.400	0.221	$0.235 \cdot 10^{-3}$	0.056	50.0	15.6	52.4	−7.5
15000	0.250	0.663	$0.774 \cdot 10^{-4}$	0.025	71.2	18.1	73.5	−10.1
15000	0.400	0.414	$0.114 \cdot 10^{-3}$	0.059	40.9	17.4	44.5	−9.1

Table 5: *CC double differential cross-section $d^2\sigma_{CC}/dxdQ^2$ and structure function term ϕ_{CC} (computed assuming $M_W = 80.4$ GeV, see eqs. 19,20) with statistical error (δ_{sta}), systematic error (δ_{sys}), and total error (δ_{tot}). The correction δ_{CC}^{qed} due to QED radiation effects, as defined in eq. 9, is also given. The normalization uncertainty, which is not included in the systematic error, is 1.5%.*

Q^2 (GeV^2)	$d\sigma_{NC}/dQ^2$ ($\mathrm{pb/GeV}^2$) $y < 0.9$ $E'_e > 11\mathrm{GeV}$	$d\sigma_{NC}/dQ^2$ ($\mathrm{pb/GeV}^2$) $y < 0.9$	δ_{sta} (%)	δ_{unc} (%)	δ_{cor} (%)	δ_{tot} (%)
200	$0.163 \cdot 10^{2}$	$0.176 \cdot 10^{2}$	0.9	3.0	1.0	3.3
250	$0.965 \cdot 10^{1}$	$0.104 \cdot 10^{2}$	0.8	3.0	0.8	3.2
300	$0.625 \cdot 10^{1}$	$0.670 \cdot 10^{1}$	0.9	3.2	1.0	3.4
400	$0.313 \cdot 10^{1}$	$0.332 \cdot 10^{1}$	1.1	2.9	1.0	3.2
500	$0.185 \cdot 10^{1}$	$0.194 \cdot 10^{1}$	1.2	2.8	1.0	3.2
650	$0.995 \cdot 10^{0}$	$0.103 \cdot 10^{1}$	1.5	2.9	1.2	3.5
800	$0.608 \cdot 10^{0}$	$0.616 \cdot 10^{0}$	1.7	2.9	1.1	3.6
1000	$0.347 \cdot 10^{0}$	$0.347 \cdot 10^{0}$	2.0	2.8	0.8	3.6
1200	$0.211 \cdot 10^{0}$	$0.211 \cdot 10^{0}$	2.4	2.8	0.9	3.8
1500	$0.112 \cdot 10^{0}$	$0.112 \cdot 10^{0}$	3.0	2.8	1.0	4.2
2000	$0.541 \cdot 10^{-1}$	$0.541 \cdot 10^{-1}$	3.5	3.0	1.1	4.8
3000	$0.188 \cdot 10^{-1}$	$0.188 \cdot 10^{-1}$	3.4	2.8	0.9	4.5
5000	$0.389 \cdot 10^{-2}$	$0.389 \cdot 10^{-2}$	5.0	3.5	0.9	6.2
8000	$0.987 \cdot 10^{-3}$	$0.987 \cdot 10^{-3}$	7.9	4.9	1.5	9.4
12000	$0.158 \cdot 10^{-3}$	$0.158 \cdot 10^{-3}$	18.3	7.9	1.7	20.0
20000	$0.386 \cdot 10^{-4}$	$0.386 \cdot 10^{-4}$	28.1	12.7	2.4	30.9
30000	$0.656 \cdot 10^{-5}$	$0.656 \cdot 10^{-5}$	71.2	18.1	3.3	73.6

Table 6: *NC cross-section $d\sigma_{NC}/dQ^2$ as measured for $y < 0.9$ and $E'_e > 11$ GeV and after correction according to SM expectations for the influence of the E'_e cut. The statistical error (δ_{sta}), the correlated systematic error (δ_{cor}), the uncorrelated systematic error (δ_{unc}) and the total error (δ_{tot}) of the $d\sigma_{NC}/dQ^2, y < 0.9$ measurement are also given. The normalization uncertainty, which is not included in the systematic error, is 1.5%.*

Q^2 (GeV^2)	$d\sigma_{CC}/dQ^2$ ($\mathrm{pb/GeV}^2$) $0.03 < y < 0.85$ $p_T^\nu > 12$ GeV	$d\sigma_{CC}/dQ^2$ ($\mathrm{pb/GeV}^2$) $y < 0.9$	δ_{sta} (%)	δ_{unc} (%)	δ_{cor} (%)	δ_{tot} (%)	δ_{qed} (%)
300	$0.164 \cdot 10^{-1}$	$0.226 \cdot 10^{-1}$	14.5	9.3	7.3	18.8	$+3.5$
500	$0.165 \cdot 10^{-1}$	$0.193 \cdot 10^{-1}$	10.0	7.7	5.8	14.0	-0.1
1000	$0.113 \cdot 10^{-1}$	$0.118 \cdot 10^{-1}$	8.2	6.6	3.7	11.4	-2.3
2000	$0.472 \cdot 10^{-2}$	$0.484 \cdot 10^{-2}$	8.4	6.2	2.4	10.9	-3.4
3000	$0.247 \cdot 10^{-2}$	$0.255 \cdot 10^{-2}$	9.6	6.3	2.2	11.8	-6.6
5000	$0.794 \cdot 10^{-3}$	$0.823 \cdot 10^{-3}$	13.1	7.3	2.5	15.3	-9.0
8000	$0.220 \cdot 10^{-3}$	$0.230 \cdot 10^{-3}$	21.4	10.8	6.2	24.9	-11.6
15000	$0.382 \cdot 10^{-4}$	$0.405 \cdot 10^{-4}$	33.4	15.3	7.9	37.7	-17.9

Table 7: *CC cross-section $d\sigma_{CC}/dQ^2$ as measured for $0.03 < y < 0.85$ and $p_T^\nu > 12$ GeV, and after correction according to SM expectations to $y < 0.9$ and for the influence of the p_T^ν cut. The statistical error (δ_{sta}), the correlated systematic error (δ_{cor}), the uncorrelated systematic error (δ_{unc}) and the total error (δ_{tot}) of the $d\sigma_{CC}/dQ^2, y < 0.9$ measurement are given. The correction due to QED radiation effects, as defined with the same convention as in eq. 9, is also given. The normalization uncertainty, which is not included in the systematic error, is 1.5%.*

Q^2 (GeV^2)	x	$\tilde{\sigma}_{NC}$	δ_{tot} (%)	δ_{sta} (%)	δ_{unc} (%)	δ_{unc}^{E} (%)	δ_{unc}^{θ} (%)	δ_{unc}^{h} (%)	δ_{cor} (%)	$\delta_{cor}^{E^+}$ (%)	$\delta_{cor}^{\theta^+}$ (%)	$\delta_{cor}^{h^+}$ (%)	$\delta_{cor}^{N^+}$ (%)	$\delta_{cor}^{B^+}$ (%)
150	.0032	1.240	5.5	1.8	4.9	1.1	0.8	0.7	1.7	−1.0	−0.4	0.4	1.1	−0.4
150	0.005	1.100	3.8	1.8	3.3	0.2	0.7	0.1	0.6	−0.2	0.4	−0.1	0.3	−0.1
150	0.008	0.920	9.3	2.9	7.9	4.0	5.6	0.2	4.1	−2.9	2.8	−0.1	−0.5	0.0
200	0.005	1.102	5.3	1.8	4.7	0.3	0.6	1.1	1.7	−0.4	−0.3	0.7	1.4	−0.3
200	0.008	0.915	4.0	1.9	3.3	0.9	0.9	0.5	1.2	0.6	−0.5	0.2	0.9	0.0
200	0.013	0.765	4.3	2.2	3.5	0.5	1.7	0.3	1.0	−0.4	0.8	0.0	0.3	0.0
200	0.020	0.696	5.5	2.6	4.6	2.2	2.3	0.6	1.7	−1.0	1.1	−0.3	−0.7	0.0
200	0.032	0.601	8.1	3.2	6.6	3.5	4.3	0.7	3.6	−2.3	2.1	−0.4	−1.7	0.0
200	0.050	0.516	9.0	3.7	7.3	4.6	4.3	0.2	3.7	−2.9	2.1	−0.3	−0.5	0.0
200	0.080	0.439	9.9	4.2	7.7	4.0	5.2	1.3	4.5	−3.2	2.6	−0.8	−1.8	0.0
250	0.005	1.113	5.6	2.3	4.9	0.3	1.3	0.7	1.3	−0.4	−0.7	0.3	0.8	−0.5
250	0.008	1.018	4.2	2.0	3.4	0.2	0.8	1.0	1.6	0.2	−0.4	0.6	1.4	−0.1
250	0.013	0.807	4.4	2.1	3.5	0.8	1.3	0.6	1.7	0.3	−0.7	0.3	1.5	0.0
250	0.020	0.721	4.1	2.1	3.5	1.2	0.7	0.3	0.9	0.6	−0.4	0.2	0.6	0.0
250	0.032	0.606	4.3	2.2	3.5	1.4	0.7	0.2	0.9	0.7	−0.3	−0.1	0.3	0.0
250	0.050	0.529	4.2	2.4	3.4	0.8	0.1	0.1	0.6	0.2	−0.1	0.1	0.6	0.0
250	0.080	0.430	4.5	2.7	3.4	0.3	0.6	0.4	1.1	0.5	−0.3	−0.5	0.7	0.0
250	0.130	0.334	5.5	3.4	4.1	0.9	0.3	1.6	1.5	0.7	−0.2	−1.0	−0.8	0.0
250	0.250	0.240	8.1	3.3	4.8	2.1	0.9	2.2	5.7	0.7	0.5	−1.3	−5.4	0.0
250	0.400	0.122	13.4	5.9	5.6	2.6	1.2	2.3	10.7	1.8	−0.6	−1.3	−10.5	0.0
300	0.005	1.139	6.5	3.4	5.2	1.8	0.3	0.2	2.0	−1.8	−0.2	−0.2	0.0	−0.6
300	0.008	0.989	5.7	2.4	4.9	0.1	1.1	1.1	1.5	0.0	−0.6	0.6	1.2	−0.2
300	0.013	0.846	4.5	2.4	3.4	0.6	1.0	0.7	1.6	0.5	−0.5	0.5	1.4	0.0
300	0.020	0.740	4.6	2.4	3.6	1.1	1.3	0.6	1.4	0.8	−0.7	0.3	1.0	0.0
300	0.032	0.629	4.4	2.4	3.5	1.3	0.7	0.4	1.1	0.7	−0.4	0.4	0.7	0.0
300	0.050	0.499	4.5	2.6	3.5	1.2	0.8	0.3	0.8	0.4	−0.4	0.3	0.6	0.0
300	0.080	0.456	4.8	2.7	3.8	1.6	0.9	0.4	1.1	0.6	−0.5	−0.2	0.8	0.0
300	0.130	0.346	6.8	3.4	5.3	3.3	1.5	1.5	2.5	2.2	−0.8	−0.8	−0.4	0.0
300	0.250	0.250	8.7	3.1	6.2	4.4	1.9	2.1	5.2	2.6	−1.0	−1.1	−4.3	0.0
300	0.400	0.140	15.6	5.7	8.8	6.8	2.0	3.6	11.6	4.5	−1.0	−2.4	−10.3	0.0
400	0.008	0.976	6.0	3.1	4.9	0.5	0.8	1.0	1.4	−0.5	−0.4	0.7	1.0	−0.5
400	0.013	0.841	4.8	2.8	3.6	0.5	1.1	1.0	1.6	0.4	−0.6	0.7	1.3	−0.1
400	0.020	0.739	4.7	2.8	3.4	0.2	0.7	0.9	1.5	−0.1	−0.3	0.5	1.3	0.0
400	0.032	0.619	4.6	2.8	3.4	0.8	0.8	0.3	0.9	0.7	−0.4	0.1	0.4	0.0
400	0.050	0.513	4.8	3.0	3.6	1.0	0.9	0.2	1.2	1.0	−0.5	−0.1	0.3	0.0
400	0.080	0.455	5.1	3.1	3.6	0.5	1.1	0.5	1.7	0.3	−0.5	0.3	1.6	0.0
400	0.130	0.373	5.9	3.8	4.2	1.5	0.9	1.0	1.7	1.4	−0.5	−0.9	−0.2	0.0
400	0.250	0.241	7.4	3.5	4.9	2.6	0.9	2.2	4.3	2.4	−0.5	−1.1	−3.4	0.0
400	0.400	0.155	13.2	6.2	5.8	3.2	0.5	2.8	10.0	2.9	−0.2	−1.8	−9.4	0.0
500	0.008	1.026	6.6	4.2	5.0	0.5	0.6	0.1	0.9	−0.5	−0.3	−0.1	0.3	−0.7
500	0.013	0.906	6.2	3.3	5.0	0.3	0.8	1.2	1.5	0.4	−0.4	0.7	1.2	−0.3
500	0.020	0.792	5.2	3.3	3.7	0.8	1.2	0.7	1.3	0.7	−0.6	0.3	0.9	0.0
500	0.032	0.654	5.2	3.3	3.6	0.4	0.4	1.3	1.7	−0.4	−0.2	0.6	1.5	0.0
500	0.050	0.508	5.4	3.5	3.8	1.3	1.0	0.4	1.6	1.4	−0.5	0.2	0.4	0.0
500	0.080	0.445	5.2	3.6	3.7	0.2	1.0	0.3	0.8	0.3	−0.5	0.2	0.4	0.0
500	0.130	0.368	6.1	4.3	4.0	1.1	0.4	0.7	1.5	1.0	0.2	−0.7	0.8	0.0
500	0.180	0.287	7.3	4.9	4.9	1.8	1.3	1.9	2.3	1.9	−0.7	−1.2	0.3	0.0
500	0.250	0.220	10.4	5.9	5.3	2.5	1.5	1.9	6.6	2.5	−0.8	−0.9	−6.0	0.0
500	0.400	0.143	17.5	8.6	8.6	5.0	1.5	5.1	12.6	5.2	−0.8	−2.8	−11.1	0.0
650	0.013	0.903	5.9	4.0	3.8	1.0	0.5	1.4	2.0	−1.1	0.2	0.9	1.3	−0.5
650	0.020	0.718	5.7	4.1	3.7	0.7	0.6	1.0	1.4	0.7	−0.3	0.4	1.1	−0.2
650	0.032	0.633	5.7	4.0	3.7	0.7	0.9	0.7	1.6	0.8	−0.5	0.4	1.2	0.0
650	0.050	0.521	5.7	4.1	3.8	0.9	0.9	0.5	1.1	0.8	−0.5	0.4	0.4	0.0
650	0.080	0.436	5.7	4.0	3.8	1.1	0.5	0.2	1.2	1.1	−0.3	0.1	0.6	0.0
650	0.130	0.413	6.6	4.6	4.4	1.1	1.7	0.1	1.6	1.1	−0.9	−0.2	0.8	0.0
650	0.180	0.309	7.9	5.3	5.2	2.3	1.3	1.7	2.7	2.5	−0.6	−0.8	−0.2	0.0
650	0.250	0.246	10.6	6.2	6.2	3.5	0.8	2.9	6.1	3.6	−0.4	−1.6	−4.7	0.0
650	0.400	0.125	15.2	9.9	7.3	3.9	0.7	3.9	9.0	3.9	−0.3	−1.9	−7.8	0.0
650	0.650	0.021	21.3	14.3	7.8	2.8	2.8	1.9	13.7	2.9	−1.4	−0.9	−13.2	0.0
800	0.013	1.000	6.8	5.0	4.4	0.4	2.2	0.4	1.7	0.8	−1.1	0.1	0.7	−0.6
800	0.020	0.796	6.3	4.6	4.0	0.6	0.9	1.4	1.6	0.6	0.4	0.9	1.1	−0.3
800	0.032	0.709	6.0	4.5	3.8	0.8	0.8	0.6	1.4	0.8	−0.4	0.6	0.9	0.0
800	0.050	0.540	6.0	4.6	3.8	0.4	0.9	0.8	1.0	0.5	−0.4	0.3	0.6	0.0
800	0.080	0.474	6.2	4.6	3.9	0.5	1.1	0.4	1.4	0.4	−0.6	−0.3	1.2	0.0
800	0.130	0.370	7.2	5.4	4.4	1.5	0.8	0.7	1.8	1.7	−0.4	−0.4	−0.2	0.0
800	0.180	0.333	7.8	6.0	4.7	1.4	1.1	1.2	1.6	1.3	−0.5	−0.5	−0.6	0.0
800	0.250	0.208	9.4	7.5	4.9	2.1	1.4	1.1	2.9	1.9	−0.7	−0.6	−2.0	0.0
800	0.400	0.150	14.2	9.6	6.9	3.0	0.8	4.2	8.0	3.3	0.4	−2.6	−6.8	0.0
800	0.650	0.018	26.9	19.6	9.8	4.8	0.9	4.8	15.5	4.8	−0.5	−2.9	−14.5	0.0

Table 8: *NC reduced cross-section $\tilde{\sigma}_{NC}(x,Q^2)$ with total error (δ_{tot}), statistical error (δ_{sta}), uncorrelated systematic error (δ_{unc}), and its contributions from the positron energy error (δ^{E}_{unc}), the polar positron angle error(δ^{θ}_{unc}) and the hadronic energy error (δ^{h}_{unc}). The effect of the other uncorrelated errors, as described in section 3.4, is included in δ_{unc}. Also given are the correlated systematic error (δ_{cor}), and its contributions from a positive variation of one standard deviation of the positron energy error ($\delta^{E^+}_{cor}$), of the polar positron angle error ($\delta^{\theta^+}_{cor}$), of the hadronic energy error ($\delta^{h^+}_{cor}$), of the error due to the noise subtraction ($\delta^{N^+}_{cor}$) and of the error due to the background subtraction ($\delta^{B^+}_{cor}$). The normalization uncertainty, which is not included in the systematic error, is 1.5%. The table continues on the next page.*

Q^2 (GeV^2)	x	$\tilde{\sigma}_{NC}$	δ_{tot} (%)	δ_{sta} (%)	δ_{unc} (%)	δ^E_{unc} (%)	δ^θ_{unc} (%)	δ^h_{unc} (%)	δ_{cor} (%)	δ^{E+}_{cor} (%)	$\delta^{\theta+}_{cor}$ (%)	δ^{h+}_{cor} (%)	δ^{N+}_{cor} (%)	δ^{B+}_{cor} (%)
1000	0.020	0.754	6.6	5.4	3.7	0.3	1.1	1.1	1.2	−0.2	−0.6	0.7	0.6	−0.5
1000	0.032	0.639	6.9	5.6	3.6	0.6	0.5	1.2	2.0	0.6	−0.3	0.7	1.7	−0.1
1000	0.050	0.566	6.4	5.1	3.6	0.7	1.1	0.9	1.0	−0.6	−0.6	0.3	0.4	0.0
1000	0.080	0.431	6.5	5.3	3.5	0.2	0.7	0.6	1.3	0.2	−0.4	0.7	1.0	0.0
1000	0.130	0.385	7.7	6.1	4.2	1.7	1.0	1.0	2.1	1.8	−0.5	−0.8	−0.8	0.0
1000	0.180	0.341	7.9	6.7	4.0	0.9	0.4	0.8	1.5	0.9	−0.2	−0.6	1.1	0.0
1000	0.250	0.244	9.5	7.8	4.6	1.5	0.9	1.7	2.8	1.8	−0.5	−1.1	−1.8	0.0
1000	0.400	0.111	18.1	12.1	9.1	5.4	2.3	5.3	9.9	5.3	−1.2	−2.3	−7.9	0.0
1000	0.650	0.013	29.2	25.0	9.5	4.1	2.6	4.6	11.7	4.2	−1.3	−3.3	−10.3	0.0
1200	0.020	0.737	8.1	7.2	3.5	0.6	0.6	1.0	1.1	−0.4	−0.3	0.5	0.6	−0.6
1200	0.032	0.645	7.4	6.4	3.5	0.4	0.3	1.4	1.5	−0.4	0.1	0.8	1.1	−0.2
1200	0.050	0.531	6.9	6.0	3.4	0.2	0.7	1.0	0.8	−0.1	−0.3	0.3	0.7	0.0
1200	0.080	0.448	6.9	5.9	3.4	0.8	0.5	0.6	1.3	0.8	−0.3	0.6	0.7	0.0
1200	0.130	0.391	7.8	6.8	3.5	0.8	0.5	0.1	1.1	0.7	−0.3	0.3	0.8	0.0
1200	0.180	0.338	8.9	7.5	4.3	1.9	1.3	0.9	2.1	1.8	−0.6	−0.7	0.4	0.0
1200	0.250	0.250	10.9	8.7	5.3	2.9	0.4	2.5	4.1	3.0	0.2	−1.2	−2.5	0.0
1200	0.400	0.129	14.8	12.1	5.7	3.4	0.8	2.1	6.3	3.6	−0.4	−1.8	−4.8	0.0
1200	0.650	0.017	29.9	24.2	11.1	5.8	1.6	6.9	13.6	5.9	−0.8	−3.4	−11.7	0.0
1500	0.020	0.789	10.5	9.2	4.8	2.7	0.6	1.0	1.7	−0.7	−0.3	−1.0	−0.6	−0.9
1500	0.032	0.581	9.2	8.1	4.0	0.6	1.2	1.7	1.7	−0.2	−0.6	1.1	1.0	−0.4
1500	0.050	0.486	8.1	7.2	3.6	0.4	0.7	1.2	1.4	0.4	−0.3	0.7	1.1	−0.1
1500	0.080	0.457	7.8	6.8	3.5	0.9	0.7	0.3	1.0	0.9	−0.4	0.2	0.2	0.0
1500	0.130	0.376	8.9	8.0	3.7	0.7	0.5	0.6	1.3	0.6	−0.2	0.3	1.0	0.0
1500	0.180	0.345	9.6	8.6	4.0	0.9	0.8	0.8	1.2	1.1	0.4	0.2	−0.4	0.0
1500	0.250	0.268	11.0	9.4	4.9	2.6	0.8	1.6	3.1	2.7	−0.4	−1.1	−1.0	0.0
1500	0.400	0.110	16.6	14.6	5.9	2.8	0.3	3.0	5.1	2.8	−0.2	−1.8	−3.9	0.0
1500	0.650	0.009	42.6	37.8	13.1	8.0	1.6	7.4	14.6	7.9	−0.8	−4.7	−11.3	0.0
2000	0.032	0.614	9.9	9.0	4.0	1.3	0.5	0.8	1.0	−0.4	−0.3	0.4	0.5	−0.7
2000	0.050	0.541	9.7	8.7	4.0	0.5	0.3	1.5	1.5	0.1	−0.2	1.1	1.0	−0.3
2000	0.080	0.428	9.1	8.3	3.7	0.1	0.2	1.0	1.1	0.4	0.1	0.4	1.0	0.0
2000	0.130	0.340	10.6	9.6	4.1	1.4	0.4	0.4	1.4	1.3	−0.2	−0.2	−0.3	0.0
2000	0.180	0.331	11.1	10.1	4.5	1.5	1.1	0.7	1.8	1.4	−0.6	0.6	0.7	0.0
2000	0.250	0.249	12.2	10.7	5.1	2.5	0.7	1.8	3.0	2.5	−0.3	−1.2	−1.1	0.0
2000	0.400	0.114	17.2	15.1	6.5	3.7	0.9	2.9	5.1	3.8	0.5	−1.7	−2.9	0.0
2000	0.650	0.011	42.2	37.8	13.2	7.2	1.0	7.9	13.3	7.3	0.5	−4.4	−10.3	0.0
3000	0.050	0.513	8.4	7.3	3.8	0.8	0.6	1.5	1.4	0.7	−0.3	0.8	0.6	−0.6
3000	0.080	0.458	8.7	7.7	4.0	0.6	0.5	1.7	1.3	−0.5	−0.2	0.9	0.7	−0.2
3000	0.130	0.347	10.2	9.1	4.3	2.1	0.5	0.1	2.1	2.0	−0.2	0.1	0.6	0.0
3000	0.180	0.324	10.0	9.2	4.0	0.3	0.4	0.6	1.0	0.6	−0.2	0.3	0.7	0.0
3000	0.250	0.242	11.1	9.9	4.4	2.1	0.2	0.7	2.2	2.1	−0.1	−0.4	−0.5	0.0
3000	0.400	0.127	15.4	12.5	7.1	4.6	0.6	3.5	5.6	4.7	−0.3	−2.2	−2.1	0.0
3000	0.650	0.012	33.6	30.1	10.9	7.0	0.5	5.2	10.2	6.2	−0.3	−3.2	−7.4	0.0
5000	0.080	0.353	11.4	10.4	4.4	1.0	0.6	1.7	1.6	0.3	−0.3	1.1	0.9	−0.7
5000	0.130	0.392	11.6	10.4	4.8	2.0	0.6	0.6	1.6	1.4	−0.3	0.4	0.5	−0.3
5000	0.180	0.223	14.1	13.4	4.5	0.9	0.2	0.5	0.6	0.5	−0.1	0.2	0.2	−0.1
5000	0.250	0.217	15.4	13.9	6.4	4.5	0.6	0.3	1.6	1.4	−0.3	−0.1	0.6	0.0
5000	0.400	0.127	19.3	17.1	7.8	5.6	0.4	2.5	4.0	3.3	0.2	−1.4	−1.9	0.0
5000	0.650	0.012	40.6	37.8	13.8	10.1	2.4	4.4	5.7	4.2	1.2	−2.6	−2.7	0.0
8000	0.130	0.283	17.2	16.5	4.7	0.5	0.5	1.5	1.4	0.2	−0.2	0.8	0.9	−0.6
8000	0.180	0.284	16.7	15.5	6.1	3.9	0.3	1.8	2.0	1.4	−0.1	0.9	1.1	−0.4
8000	0.250	0.273	16.6	15.1	6.6	4.8	0.7	0.5	2.5	2.3	0.3	−0.5	−0.7	−0.2
8000	0.400	0.093	26.2	24.2	9.8	8.5	0.7	0.4	1.5	1.4	−0.4	0.3	0.5	0.0
8000	0.650	0.013	48.9	44.7	18.3	15.6	2.4	4.8	7.5	6.3	1.2	−2.7	−3.0	0.0
12000	0.180	0.153	34.6	34.4	3.8	1.9	1.5	0.2	2.0	1.6	−0.8	−0.4	0.0	−0.7
12000	0.250	0.127	32.7	32.1	6.1	5.1	0.4	1.6	1.3	0.5	0.2	1.1	0.5	−0.4
12000	0.400	0.085	35.2	33.3	11.2	10.8	0.2	0.3	2.4	2.3	0.1	0.2	0.2	−0.1
12000	0.650	0.015	62.6	57.7	23.4	22.8	2.4	2.8	6.1	5.7	1.2	−1.6	−1.2	0.0
20000	0.250	0.090	62.2	61.9	5.1	3.1	1.6	1.6	2.1	−1.0	−0.8	−1.3	−0.2	−1.0
20000	0.400	0.142	37.0	35.7	9.6	8.8	0.4	2.3	2.2	1.3	−0.2	1.7	0.6	−0.5
20000	0.650	0.021	82.0	70.7	40.4	40.0	3.9	0.6	9.7	9.5	1.9	−0.5	−0.3	−0.1
30000	0.400	0.182	72.6	71.9	9.4	6.8	2.1	1.6	1.8	0.8	−1.0	−0.7	−0.4	−0.9

Q^2 (GeV^2)	x	$d^2\sigma/dxdQ^2$ (pb/GeV^2)	δ_{tot} (%)	δ_{sta} (%)	δ_{unc} (%)	δ^h_{unc} (%)	δ_{cor} (%)	δ^{V+}_{cor} (%)	δ^{h+}_{cor} (%)	δ^{N+}_{cor} (%)	δ^{B+}_{cor} (%)
300	0.013	$0.637 \cdot 10^{0}$	31.8	27.4	9.9	2.9	12.6	11.9	−1.6	0.2	−3.8
300	0.032	$0.124 \cdot 10^{0}$	30.0	28.1	7.9	2.8	6.6	6.2	−1.6	0.9	−0.7
300	0.080	$0.532 \cdot 10^{-1}$	25.5	23.8	7.0	2.2	2.8	2.2	−1.5	−0.6	−0.3
500	0.013	$0.468 \cdot 10^{0}$	29.7	25.1	9.2	1.9	12.8	12.1	−1.5	1.0	−3.9
500	0.032	$0.177 \cdot 10^{0}$	19.2	17.0	6.7	2.3	5.5	5.2	−1.2	0.4	−0.3
500	0.080	$0.546 \cdot 10^{-1}$	18.9	17.0	6.1	1.1	2.3	2.3	−0.5	0.2	−0.2
500	0.130	$0.289 \cdot 10^{-1}$	29.4	27.8	7.8	1.5	1.6	0.3	−1.3	−0.9	−0.1
1000	0.032	$0.124 \cdot 10^{0}$	17.1	15.0	6.5	1.8	4.7	4.6	−1.3	0.2	−0.2
1000	0.080	$0.487 \cdot 10^{-1}$	14.8	13.3	5.7	0.9	2.3	2.1	−0.8	0.6	−0.1
1000	0.130	$0.199 \cdot 10^{-1}$	22.5	20.9	6.4	0.9	1.0	0.6	−0.7	−0.4	−0.1
1000	0.250	$0.105 \cdot 10^{-1}$	34.1	31.7	10.4	3.0	5.2	0.0	3.1	−4.2	−0.1
2000	0.032	$0.716 \cdot 10^{-1}$	18.1	15.7	6.9	1.0	5.5	5.4	−1.5	1.7	−0.4
2000	0.080	$0.264 \cdot 10^{-1}$	14.8	13.5	5.6	0.1	1.7	1.6	0.3	0.3	−0.2
2000	0.130	$0.949 \cdot 10^{-2}$	21.4	20.6	5.7	0.6	0.6	0.4	0.3	0.4	−0.2
2000	0.250	$0.566 \cdot 10^{-2}$	24.6	23.0	7.0	0.4	2.2	0.1	−0.2	−2.2	−0.1
3000	0.080	$0.156 \cdot 10^{-1}$	16.8	15.2	6.2	2.3	2.7	2.1	1.5	0.7	−0.2
3000	0.130	$0.872 \cdot 10^{-2}$	18.1	17.0	5.8	1.6	1.1	0.6	0.8	0.6	−0.1
3000	0.250	$0.283 \cdot 10^{-2}$	25.1	23.6	7.8	4.7	2.6	0.1	2.5	−0.6	−0.1
5000	0.130	$0.402 \cdot 10^{-2}$	22.3	21.0	7.0	3.9	2.6	0.6	2.5	0.4	−0.1
5000	0.250	$0.111 \cdot 10^{-2}$	27.6	26.8	6.5	2.9	0.8	0.2	1.2	0.6	−0.1
8000	0.130	$0.125 \cdot 10^{-2}$	38.5	35.7	12.6	10.8	6.8	1.2	6.5	1.5	−0.3
8000	0.250	$0.530 \cdot 10^{-3}$	35.4	33.5	9.9	7.9	5.4	0.2	5.2	1.2	−0.1
8000	0.400	$0.235 \cdot 10^{-3}$	52.4	50.0	13.1	10.9	8.5	0.0	8.5	−0.8	0.0
15000	0.250	$0.774 \cdot 10^{-4}$	73.5	71.2	15.9	14.3	8.5	1.0	8.4	1.1	−0.2
15000	0.400	$0.114 \cdot 10^{-3}$	44.5	40.9	15.3	14.2	8.2	0.1	8.1	0.9	−0.1

Table 9: *CC double differential cross-section $d^2\sigma_{CC}/dxdQ^2$ with total error (δ_{tot}), statistical error (δ_{sta}), uncorrelated systematic error (δ_{unc}), and its contributions from the hadronic energy error (δ^h_{unc}). The effect of the other uncorrelated errors, as described in section 3.4, is included in δ_{unc}. Also given are the correlated systematic error (δ_{cor}), and its contributions from a positive variation of one standard deviation of the error coming from the cut on the V_{ap}/V_p ratio (δ^{V+}_{cor}), of the hadronic energy error (δ^{h+}_{cor}), of the noise contribution (δ^{N+}_{cor}) and of the estimated background contribution (δ^{B+}_{cor}). The normalization uncertainty, which is not included in the systematic error, is 1.5%.*